J. Fluid Mech. (2020), *vol.* 891, A12.
Published by Cambridge University Press

doi:10.1017/jfm.2020.134

Effective permeability tensor of confined flows with wall grooves of arbitrary shape

Mainendra Kumar Dewangan[1] **and Subhra Datta**[1,†]

[1]Department of Mechanical Engineering, Indian Institute of Technology Delhi, Hauz Khas, New Delhi 110016, India

(Received 18 September 2019; revised 31 January 2020; accepted 12 February 2020)

Pressure and shear-driven flows of a confined film of fluid overlying a periodic one-dimensional topography of arbitrary shape are considered for prediction of the effective hydraulic permeability in the Stokes flow regime. The other surface confining the fluid may be a planar no-slip wall, an identically patterned wall, a free surface or a surface with prescribed shear. Analytical predictions are obtained using spectral analysis and the domain perturbation method under the assumption of small pattern size to pitch ratio. Using a novel decomposition of the channel height effects into exponentially and algebraically decaying components, a simple surface-metrology-dependent relationship which connects the eigenvalues of the effective permeability tensor is obtained. Two representative topographies are assessed numerically: the infinitely differentiable topography of a phase-modulated sinusoid which has multiple local extrema and zero crossings and the non-differentiable triangular-wave topography. Non-differentiability in the form of corners of triangular patterns and the cusps of scalloped patterns are not found to be an impediment to meaningful and numerically accurate asymptotic predictions of effective permeability and effective slip, contradicting an earlier suggestion from the literature. Several distinct applications of the theory to the friction-reduction and shear-stability performance of the recently developed lubricant impregnated patterned surfaces as well as to scalloped and trapezoidal drag-reduction riblets are discussed, with comparison to experimental data from the literature for the last application. Analytical approximations which have an extended domain of numerical accuracy are also proposed.

Key words: Hele-Shaw flows, general fluid mechanics, drag reduction

1. Introduction

The subject of this study, a flowing film of fluid contacting a surface with complex topographic patterns, is a prominent feature of both technology and nature. Superhydrophobic surfaces (SHS) (Choi *et al.* 2006; Ybert *et al.* 2007; Zhou *et al.* 2013; Song, Daniello & Rothstein 2014) and liquid-impregnated surfaces (LIS) (Wexler, Jacobi & Stone 2015; Asmolov, Nizkaya & Vinogradova 2018; Solomon

†Email address for correspondence: subhra.datta@mech.iitd.ac.in

et al. 2018) have been shown to reduce the frictional resistance of flow passages with potential applications to microfluidics and flow batteries. An important application of SHS and LIS in the form of antimicrobial surfaces for implants and surgical instruments involve contact with flowing blood (Wong *et al.* 2011; Parmar *et al.* 2018). Similarly, contact with flowing sea water may arise in applications of SHS and LIS to prevent marine bio-fouling (Ware *et al.* 2018). In fact, the stability of LIS under shear is a specific area of concern (Wexler *et al.* 2015) for their technological viability. The anisotropy of flow over topographic patterns can be leveraged to successfully mix reagents in microfluidics (Stroock & McGraw 2004) and even to effect separations (Asmolov *et al.* 2015).

In addition to relevance to the above-discussed more recent technological advances, a substantial motivation behind studying wetted topographic patterns has historically been in the realm of reduction of skin-friction drag in turbulent flows through riblets immersed within the viscous sublayer (Bechert & Bartenwerfer 1989; Luchini, Manzo & Pozzi 1991; Choi, Moin & Kim 1993; Chang *et al.* 2019). Inspiration for this application is drawn from the micro-structure of the skin of marine organisms like fast-moving sharks. Also of relevance to the current study on confined flows is the fact that fractured rocks in natural/man-made geological formations also present complex topographies to even the laminar flow of oil and water, causing departures from the Poiseuille law that need careful consideration (Sisavath *et al.* 2003).

Corrugations provide often the smallest or the least-resolvable scale in the hierarchy of scales that affect fluid flow (Bechert & Bartenwerfer 1989; Miksis & Davis 1994; Tuck & Kouzoubov 1995; Kamrin, Bazant & Stone 2010). A powerful theoretical paradigm in the assessment of the hydrodynamic effects of wall corrugation arises from the realization that the feature-averaged effects of wall corrugations accessible to coarse-scale measurements can be quantified easily through effective equation approaches such as locating an effective no-slip plane (Tuck & Kouzoubov 1995; Kamrin *et al.* 2010) or evaluating for confined flows the hydrodynamic conductance of an equivalent channel with a simpler wall geometry (Stroock *et al.* 2002; Feuillebois, Bazant & Vinogradova 2009). The location of the effective no-slip plane, which depends of course on the reference plane for measuring distances, has been specified variously through closely related parameters such as the 'effective slip length' or the 'protrusion height', the latter term being used almost exclusively in the turbulent-drag-reduction literature (Bechert & Bartenwerfer 1989). In what follows, the above-discussed effective equation approach will play an important role.

In SHS, the liquid does not contact all points of the pattern and the details of the solid-contacting gas flow is not usually resolved (Lauga & Stone 2003; Asmolov *et al.* 2013*a*; Kumar, Datta & Kalyanasundaram 2016). In contrast, the current study will deal with a fluid contacting a solid no-slip surface. Crucially, in creeping flow, SHS (Zhou *et al.* 2013) and wetted surfaces (Lecoq *et al.* 2004) with the same pattern waveform (e.g. trapezoidal, as in the above two studies) act as drag-reducing and drag-enhancing surfaces, respectively, as judged from the location of the effective no-slip plane, which is closer to the troughs in SHS and closer to the peaks in wetted surfaces. Wetted trapezoidal surfaces such as in Lecoq *et al.* (2004) will be investigated as an application in the current study. The literature on SHS will not, therefore, be surveyed in great detail. The literature on channels with non-planar mean wall shapes will also be left out of scope.

The problem of predicting the location of the effective no-slip plane in shear flows bounded only on one side by a specialized topography such as rectangular or sinusoidal topographic patterns has attracted the attention of several researchers

over last half a century (Richardson 1973; Hocking 1976; Tuck & Kouzoubov 1995; Wang 2003, 2010; Dewangan & Datta 2019). Unconfined flows with trapezoidal, triangular and other cornered topographies having specialized analytical forms have been accessed through conformal mapping (Bechert & Bartenwerfer 1989) and semi-analytical approaches such as those based on boundary integral formulations (Luchini *et al.* 1991; Wang 2003) and spectral-asymptotic analyses (Lecoq *et al.* 2004). However, the studies by Luchini *et al.* (1991) and Kamrin *et al.* (2010) stand out for providing expressions for the effective slip in unconfined shear flows over arbitrarily shaped periodic one- and two-dimensional topographies respectively, although under the assumption of small peak height to pitch ratios. Miksis & Davis (1994) also provide an expression of similar generality using the asymptotic method of multiple scales, but at a lower order of accuracy that places the effective slip plane on the metrological 'mean line'. Einzel, Panzer & Liu (1990) and Panzer, Liu & Einzel (1992) analyse arbitrary topography shapes through a spectral approach, but only evaluate the effective slip of small-amplitude sinusoidal topographies in closed form. Luchini (2013) provides asymptotic and numerical results connecting the shear-flow predictions obtained by two distinct paths of approach to the small-amplitude limit, *viz.* fixed-pitch approach and fixed pitch-to-amplitude ratio approach. The former limit is relevant to the current study.

The current study deals with confined flow passages rather than an isolated surface. So the concept of tensorial effective permeability (or the effective friction factor) is considered to be more appropriate here than effective slip, as discussed in Feuillebois *et al.* (2009), Feuillebois, Bazant & Vinogradova (2010) for SHS and Ajdari (2001) for wetted patterns. In relation to confined pattern-wetting flows, analytically tractable results are available for planar passages with small-amplitude sinusoidal wall topography (Chu 1996; Vasudeviah & Balamurugan 1999; Stroock *et al.* 2002; Wang 2011). Pattern-wetting flows through planar passages that are thin compared to the pattern wavelength have also been studied with the help of lubrication theory (Sisavath *et al.* 2003; Sun & Ng 2017; Tavakol *et al.* 2017). The lubrication theory, despite its limitation to channel sizes much thinner than the pattern pitch, has the advantage of allowing facile specification of arbitrarily shaped wall-pattern waveforms, as leveraged by these studies. It appears that the literature lacks analytical findings on the permeability (or friction factor) of finite-thickness channels with arbitrarily specifiable wetted wall patterns. Finite-thickness channels are definitely not accessible by the 'slow-variation' approach of lubrication theory (Van Dyke 1987) and for such channels, the findings from analysis of an unconfined shear flow do not translate directly.

The approach employed to develop effective equations can also be used as a classification basis of the works relevant to the current study. For example, Richardson (1973), Tuck & Kouzoubov (1995), Scholle, Wierschem & Aksel (2004) and Bechert & Bartenwerfer (1989) realize the no-slip condition on specialized topographies using conformal maps on the complex plane which are inclusive of Schwartz–Christoffel and Kutta–Joukowski transformations. Hocking (1976) and Luchini *et al.* (1991) employ the Wiener–Hopf technique to resolve infinite groove depths. Spectral methods are employed by Einzel *et al.* (1990), Panzer *et al.* (1992) and Dewangan & Datta (2018). The asymptotic method of domain perturbations is employed by Luchini *et al.* (1991), Stroock *et al.* (2002), Wang (2003), Kamrin *et al.* (2010), Wang (2010) and Asmolov *et al.* (2018). While the works mentioned in the previous paragraph attempt to resolve the effective no-slip plane and effective friction factors analytically, a complementary set of methods furnishing numerical solutions exist for flows over corrugated surfaces.

Among them, mention may be made of molecular dynamics simulations (Guo, Chen & Robbins 2016), the finite-element method (Choudhary *et al.* 2011; Guo *et al.* 2016), the point-collocation boundary integral method (Wang 2003), finite-volume and finite-difference methods (Asako & Faghri 1987; Yutaka, Hiroshi & Faghri 1988; Schönfeld & Hardt 2004; Annepu, Sarkar & Basu 2014; Sharma *et al.* 2019), the lattice-Boltzmann method (Li & Chen 2005), dissipative particle dynamics simulations (Asmolov *et al.* 2013*b*; Zhou *et al.* 2013), multiple scattering theory and stochastic averaging (Sarkar & Prosperetti 1996). A semi-analytical spectral approach has been utilized to resolve confined flows over SHS with alternating finite-slip no-slip patterns (Zhou *et al.* 2013). The phase-field method (Chakraborty 2007), front-tracking method (Sun & Ng 2017) and volume-of-fluid method (Alamé & Mahesh 2019) have been employed to resolve interfaces in two-phase systems.

Studies which report experiments on pattern-wetting flows and use well-controlled pattern/roughness elements with precise measurement of all their significant dimensions in addition to reporting of averaged parameters such as absolute and/or the root-mean-squared roughness values (abbreviated R_a and R_q, respectively) are mostly based on rectangular ridges (Stroock *et al.* 2002; Wierschem, Scholle & Aksel 2003; Gamrat *et al.* 2008), with the exception of Lecoq *et al.* (2004), who characterize the shear and squeeze-film flows over trapezoidal patterns. Interestingly, the force on a sphere from a squeezed liquid film which is amenable to precise measurements (see e.g. Lecoq *et al.* (2004) and Mongruel *et al.* (2013) for a study on rectangular-grooved surfaces), has an interesting connection to the effective slip in shear that can be brought out through lubrication theory (Asmolov, Belyaev & Vinogradova 2011) as well as the application of the Lorenz reciprocity theorem (Lecoq *et al.* 2004). Superhydrophobic trapezoidal grooves as studied in Zhou *et al.* (2013) would reduce the net creeping-flow drag vis-à-vis a planar surface located on the mean line, while the wetted surfaces studied here (Zhou *et al.* 2013) enhance the drag. Although SHS involve two fluids, the flow field in the non-wetting fluid overlying the superhydrophobic trapezoidal grooves can be resolved analytically through a boundary-condition formalism different from wetted flows, that is based on the 'gas cushion model' (Nizkaya *et al.* 2015; Dubov *et al.* 2018). As detailed in § 4.4 as well as Zhou *et al.* (2013), the 'gas cushion model' involves application of a slip boundary condition on the plane connecting the tips of trapezoids.

The purpose of the current work is to study analytically the effect of arbitrarily shaped one-dimensional corrugation waveforms on the hydraulic permeability (or the effective conductance) of channels with sizes that are neither large enough to be accessible for treatment as a shear flow, nor small enough to be accessible for treatment through lubrication approximation. The effect of inertia will be assumed to be vanishingly small, as typical in microfluidic applications. The method of domain perturbations (Van Dyke 1987; Hinch 1991), which involves the assumption of small characteristic amplitude to wavelength ratio and the shifting of boundary conditions to a convenient reference plane, will be employed. Finite-element simulations fully resolving the Stokes flow field are used for assessment of the analytical predictions for two specific shapes of wall undulations differing in their degree of smoothness. To enable the evaluation of the permeability when flow is oblique to the patterns, permeability will be evaluated in both the principal directions, i.e. in longitudinal flow where the applied pressure differential (or shear) is aligned along the pattern, and in transverse flow, where the applied forces are aligned across the pattern. Several new and convenient analytical results will be derived and validated for numerical accuracy. A hitherto unreported universal relationship valid for any prescribed periodic surface

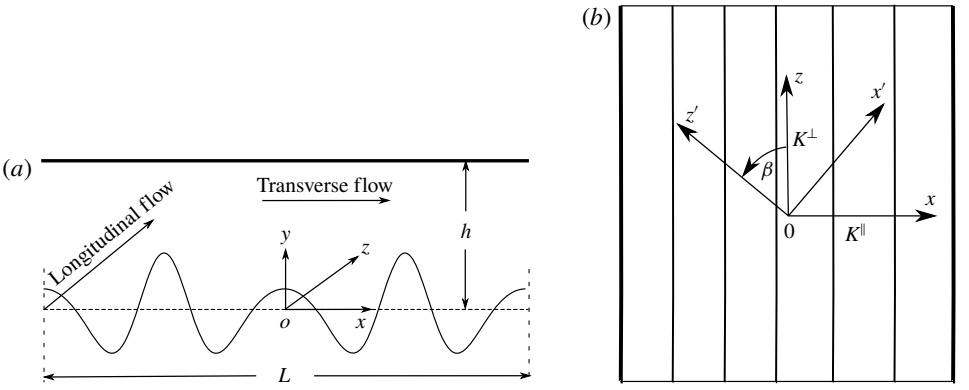

FIGURE 1. Panel (*a*) shows longitudinal/transverse flow through a channel with an arbitrarily shaped pattern on the bottom wall and a flat top wall. The pattern wavelength and the mean height of the channel is L and h, respectively. Panel (*b*) shows local coordinate systems xoz and $x'oz'$ with the ordinates aligned with the stripes and at an angle β to the stripes, respectively. The permeabilities along and across the pattern direction are $K_{\parallel}$ and $K_{\perp}$, respectively.

profile in confined flow, along the lines of those already known for the effective slip of isolated surfaces with patterned hydrodynamic slippage (Asmolov & Vinogradova 2012), which enables easy evaluation of permeability in the second principal direction once the permeability in the first principal direction is known, will be derived.

In § 2 a canonical confined flow problem, which is to be solved with arbitrary wall topography shape and arbitrary height is defined. In § 3 the hydraulic permeability is evaluated in longitudinal and transverse flow. A relationship is derived in this section between the components of the diagonalized permeability tensor. Section 3 also discusses the adaptation of the theory to other boundary conditions and flow configurations arising in applications. Section 4 specializes the analysis to specific test topographies, assesses the numerical accuracy of the asymptotic predictions and also discusses two distinct applications of the theory in the currently active area of slippery lubricant infused patterned surfaces placed in a dynamic fluid environment. This section also performs an experimental comparison with data from a complex topography studied in the literature. Section 5 discusses the main conclusions from the current work.

2. Problem definition

Incompressible laminar flow of a Newtonian fluid of viscosity μ and density ρ is considered. The periodic cell of the channel through which the flow occurs is shown in figure 1(*a*). The lower wall is patterned topographically and can be located by the function $y = eg(x)$, where e is a characteristic amplitude of the L-periodic pattern specified by the function $g(x)$. The channel has a flat wall at $y = h$. No-slip boundary condition is considered to apply on both the walls. The reference plane ($y = 0$) from which the ordinate $g(x)$ is measured is chosen to be the 'mean line', to borrow a nomenclature from surface metrology (Whitehouse 1994). By this definition, $g(x)$ has to satisfy $\int_{-L/2}^{L/2} g(x)\,\mathrm{d}x = 0$. The nominal thickness of the channel measured from the

mean line is denoted by h. The flow is considered to be driven by a pressure drop ΔP although extensions to shear-driven flow are discussed in and onward from § 3.4. The velocity components along the rectangular Cartesian coordinates x, y, z (figure 1*a*) are denoted by u, v, w and the pressure is denoted by p.

A channel configuration with an unpatterned wall opposing a patterned wall, as shown in figure 1(*a*), is often preferred in microfluidic experiments from considerations such as ease of alignment (Feuillebois *et al.* 2009) and/or optical access (Devasenathipathy, Santiago & Takehara 2002). While details of the analysis are demonstrated through the configuration in figure 1(*a*), several other confined flow configurations are studied later in § 3.4. It can be noted here that the geometry of figure 1(*a*) is also used by Stroock *et al.* (2002) with a cosine shaped topography ($g(x) = \cos(x)$). Our subsequent findings would reduce to those of Stroock *et al.* (2002) as special cases, providing partial validation of our results.

In the following, the inertia of the fluid will be neglected so that the flow is governed by the Stokes equations, as appropriate for microfluidic applications where the Reynolds number based on the characteristic size of the channel is small (Stone, Stroock & Ajdari 2004). There are also situations where physical and/or scaling arguments can justify the neglect of inertia in spite of a finite value of the Reynolds number based on the nominal channel height. These include unidirectional flow situations, e.g. when the periodic cell of figure 1(*a*) is located sufficiently far from entrances/exits and other disturbances to the flow, with the flow being directed parallel to the corrugations (longitudinal flow), as in § 3.1. Inertial effects can also be neglected on scaling grounds in the limiting situation of the channel size being an infinitesimal fraction of the patterning wavelength (Van Dyke 1987). Interestingly, the flow within the viscous sublayer of a turbulent external flow has been modelled as a zero-inertia flow by Bechert & Bartenwerfer (1989) and Luchini *et al.* (1991).

The following dimensionless variables are introduced for use in the rest of the article: $x = (L/2\pi)X$, $y = (L/2\pi)Y$, $u = (U_s)U$, $v = (U_s)V$, $w = (U_s)W$, $p = (\Delta p/2\pi)P$, where the velocity scale U_s will be specified shortly. The symbol $\boldsymbol{\nabla}$ will signify the dimensionless gradient operator in the plane (x–y) of the topographic pattern. Incidentally, following the above non-dimensionalization scheme, the ratio of the inertia to viscous terms in the full Navier–Stokes equation would scale as Re/H, where $Re = \rho U_s h/\mu$. The neglect of inertia will either require a strict Stokes flow assumption, or that $1/H$ be vanishingly small in the case $Re \sim O(1)$ (or higher). Finite (but possibly large) H is an important concern in what follows and the $O(1/H)$ terms retained in the finite-H analysis are not of inertial origin. Therefore, the finite-H analysis applies only to Stokes flow and additional corrections stemming from the inertia terms would be needed for a flow where $Re \sim O(1)$ or higher. The shear-based scale $U_s = \Delta p h/2\pi\mu$ for velocity is used in the remainder of the articlehere. This scale is crucial for understanding the effect of finite channel size studied later in the article.

The concern of this article is to obtain reliable analytical (preferably closed-form) estimates of the channel hydraulic permeability in Stokes flow, in the presence of arbitrary wall patterns. The permeability (k) is defined as the volumetric flow rate of a fluid of unit viscosity in a channel subject to unit pressure gradient, and has dimensions of length squared. However, in most of the subsequent development, k will be normalized by the permeability of the corresponding channel of height h where the wall patterns are absent ($e = 0$), leading to the dimensionless permeability K. The symbol for permeability may be superscripted/subscripted where necessary to indicate flow, channel and pattern types. It may be noted that the dimensionless permeability

can also be interpreted as the ratio of the Poiseuille number of the unpatterned channel to that of the patterned channel. The Poiseuille number is proportional to the product of the Fanning/Darcy friction factor and the Reynolds number (Taylor 1971).

If the flow direction is oblique to stripes (figure 1*b*), the resultant tensorial permeability (Bazant & Vinogradova 2008; Schmieschek *et al.* 2012) is completely determined by the permeability in the two canonical directions (z and x) along and across the stripes, which are termed longitudinal and transverse flow, respectively. Further details on the tensorial nature of permeability relevant to the current study are discussed in the beginning of the next section.

3. The hydraulic permeability tensor

In an infinite Hele-Shaw cell with one-dimensional wall topography, the direction of net fluid permeation is, in general, different from the direction of applied forces (Ajdari 2001; Ghosal 2002). Let the vector $\boldsymbol{K}_\beta$ encode the magnitude of the normalized hydraulic permeability and the direction of fluid permeation. Referring to figure 1(*b*), the components of $\boldsymbol{K}_\beta$ along and perpendicular to any direction $\overrightarrow{OX'}$ oriented at an angle β with respect to the one-dimensional striped pattern can be calculated using the relation $\boldsymbol{K}_\beta = \boldsymbol{M}\hat{l}$, where $\hat{l} = (l', m')$ are the direction cosines of the applied force causing the fluid flux in the $x' - z'$ coordinate system. The tensor $\boldsymbol{M}$ is given by $\boldsymbol{M} = R_{-\beta}\,\mathrm{diag}(K_\parallel, K_\perp)R_\beta$ (Ajdari 2001; Bazant & Vinogradova 2008; Feuillebois *et al.* 2010) and will be termed the hydraulic permeability tensor here. Here, R_β is the two-dimensional matrix that rotates points in the $(x\text{–}z)$ plane by an angle β. Since the only non-geometrical parameters affecting $\boldsymbol{M}$ are $K_\parallel$ and $K_\perp$, the rest of the theoretical development is devoted to evaluating $K_{||}$ for longitudinal flow (§ 3.1) and $K_\perp$ for transverse flow (§ 3.2) by solving the respective flow problems.

3.1. *Longitudinal flow*

With respect to the longitudinal flow through the geometry shown in figure 1(*a*), the velocity $W(X, Y)$ of the unidirectional flow is governed by the balance of viscous and pressure forces while the no-slip boundary conditions apply at both the corrugated bottom wall and the flat top wall, leading to

$$\nabla^2 W = -\frac{1}{H}, \tag{3.1a}$$

$$W(X, \epsilon g(X)) = 0, \tag{3.1b}$$

$$W(X, H) = 0. \tag{3.1c}$$

Here, $\epsilon = 2\pi e/L$ and $H = 2\pi h/L$ are a characteristic pattern size and the nominal channel thickness, rendered dimensionless through multiplication with the pattern wavenumber $2\pi/L$. The H-dependent right-hand side of (3.1*a*) is a consequence of the wall-shear-based velocity scale $(\Delta p h/2\pi\mu)$.

In the following, ϵ will be treated as a small parameter, and asymptotic expansions in the form $W = W^0 + \epsilon W^1 + \epsilon^2 W^2 + o(\epsilon^2)$ together with the method of domain perturbations (Hinch 1991), which involves the transfer the boundary condition on the curved surface (3.1*b*) to $Y = 0$ through the Taylor expansion $W(X, \epsilon g(X)) = W(X, 0) + \epsilon g W_Y(X, 0) + \epsilon^2 g^2 W_{YY}(X, 0)/2 + o(\epsilon^2)$, will be employed. Here, subscripts denote derivative. Since the highest-order correction evaluated in this study is W^2, algebraic expressions for the normalized permeability derived in §§ 3, 3.4 and 4 will contain an $o(\epsilon^2)$ error term, even though the same will be indicated explicitly only when important to the discussion. The 'little o' asymptotic notation used here may be noted.

3.1.1. *Leading order* ($O(1)$)

The leading-order solution is obtained by setting $\epsilon = 0$ and corresponds to a flat bottom wall at $Y = 0$, where the X independent flow velocity W^0 is given by

$$W^0 = \frac{Y}{2} - \frac{Y^2}{2H}. \tag{3.2}$$

3.1.2. *The* $O(\epsilon)$ *correction*

The governing equation and no-slip boundary conditions for W^1 are

$$\nabla^2 W^1 = 0, \tag{3.3a}$$

$$W^1(X, 0) + g(X) W^0_Y(X, 0) = 0, \tag{3.3b}$$

$$W^1(X, H) = 0, \tag{3.3c}$$

which have the solution

$$W^1(X, Y) = \sum_{n\neq 0}^{\infty} C_{1n}(\mathrm{e}^{-|n|Y} - \mathrm{e}^{-2|n|H}\mathrm{e}^{|n|Y})\mathrm{e}^{inX}, \tag{3.4a}$$

$$C_{1n} = -\frac{g_n}{2(1 - \mathrm{e}^{-2|n|H})}. \tag{3.4b}$$

In (3.4*a*) and the remainder of the article, a summation symbol subscripted with $n \neq 0$ denotes a sum taken through all integers except zero.

3.1.3. *The* $O(\epsilon^2)$ *correction*

The governing equation and no-slip boundary conditions for W^2 are

$$\nabla^2 W^2 = 0, \tag{3.5a}$$

$$W^2(X, 0) + g(X) W^1_Y(X, 0) + \frac{g(X)^2}{2} W^0_{YY}(X, 0) = 0, \tag{3.5b}$$

$$W^2(X, H) = 0, \tag{3.5c}$$

for which it is sufficient for the purpose of obtaining an $O(\epsilon^2)$-accurate prediction of the permeability, to find an expression for the period-averaged velocity $\langle W^2(X, Y)\rangle$, which is the part of W_2 obtained by excluding its harmonic ($\propto \mathrm{e}^{inX}, n \neq 0$) parts. The quantity $\langle W^2(X, Y)\rangle$ is given by

$$\langle W^2(X, Y)\rangle = C^{\parallel}\left(1 - \frac{Y}{H}\right), \tag{3.6a}$$

$$C^{\parallel} = -S_1^{\parallel} + \frac{S_2}{H}, \tag{3.6b}$$

$$S_1^{\parallel} = \sum_{n=1}^{\infty} n \coth(nH)|g_n|^2, \tag{3.6c}$$

$$S_2 = \sum_{n=1}^{\infty} |g_n|^2. \tag{3.6d}$$

The series $S_1^{\parallel}$ arises from convolution of the Fourier series of g into that of its y derivative and for a given surface topography, its convergence is crucial to obtaining meaningful answers from the domain perturbation method. The series S_2 converges to $1/4\pi$ times the variance of the topography, as per Parseval's identity.

3.1.4. *Effective permeability*

The effective dimensionless permeability K is obtained from the dimensionless flow rate $Q(\epsilon, H)$ using its definition discussed in § 2, which leads to $K = Q(\epsilon, H)/Q(0, H)$. Here, the functional argument of Q within parentheses indicate the dependence of Q on ϵ and H. In longitudinal flow, Q is obtained from an $O(\epsilon^2)$-accurate Taylor-series approximation of

$$Q^{\parallel}(\epsilon, H) = \int_{-\pi}^{\pi}\int_{\epsilon g(X)}^{H} W \,\mathrm{d}Y\,\mathrm{d}X = \int_{-\pi}^{\pi}\int_{\epsilon g(X)}^{H} [W^0 + \epsilon W^1 + \epsilon^2\langle W^2\rangle + o(\epsilon^2)]\,\mathrm{d}Y\,\mathrm{d}X. \quad (3.7)$$

As discussed below equation (3.5), the harmonic parts of W_2 do not contribute to the $O(\epsilon^2)$-accurate flow rate.

Below, we first provide expressions for K which are applicable to arbitrary channel height. Then, at the cost of errors that decay exponentially fast with H, we derive expressions for large but finite channel height that are simpler and often more tractable in closed form. Below, a 'relative roughness' parameter $\alpha = e/h = \epsilon/H$ is introduced in the expressions for K in favour of ϵ as one of the independent variables, borrowing familiar terminology from the celebrated Moody chart for the Darcy–Weisbach friction factor (Taylor 1971) and notation from the study on sinusoidal patterns by Stroock *et al.* (2002).

For arbitrary channel height. The following expressions for the normalized permeability are obtained on integrating W using (3.7) to $O(\epsilon^2)$ accuracy:

$$K_{\parallel} = 1 - 6\alpha^2(HS_1^{\parallel} - S_2) + o(\epsilon^2). \quad (3.8)$$

For the special case of $g(x) = \cos(x)$, equation (3.8) reduces to a scaled version of (13) from Stroock *et al.* (2002), reassuring our H-dependent calculations.

Exponentially accurate approximation of the effect of finite channel height. The nominally 'large H' approximation to be discussed now is one of the important contributions of the current study. It amounts to setting to zero all terms that signify integral powers of e^{-H} in the preceding expressions, without altering any terms that decay algebraically with H, i.e. the terms containing integral powers of $1/H$. The important consequences from this limiting process are

$$W^1(X, Y) = \frac{1}{2}\sum_{n\neq 0}^{\infty} g_n \mathrm{e}^{-|n|Y}\mathrm{e}^{\mathrm{i}nX} + e.s.t.(H), \quad (3.9a)$$

$$C^{\parallel} = -S_1 + \frac{S_2}{H} + e.s.t.(H) = -S_1 + O(1/H), \quad (3.9b)$$

$$S_1 = \sum_{n=1}^{\infty} n|g_n|^2 \quad (3.9c)$$

and that W^2 still continues to be given by (3.6).

In (3.9) and the remainder of the article, the abbreviation $e.s.t.(H)$ signifies terms that decrease exponentially fast with increase of H, i.e. 'exponentially small terms' at large H. The $e.s.t.(H)$ always arise in the contribution from non-zero wavenumbers in the dependent variables, i.e. in their harmonic ($n \neq 0$) parts. The convergence of the sum S_1 is crucial to the meaningfulness of large H predictions.

The first equality of (3.9*b*) pertains to the large-H approximation promulgated in the current work. The intuitively 'cruder' algebraically accurate estimate of $C^{\parallel}$ given by the second equality of (3.9*b*) will also be discussed shortly and later subject to numerical evaluations.

In terms of the steps followed in §§ 3.1.1–3.1.3, the neglect of $e.s.t.(H)$ terms in the manner discussed above leaves the governing equations and the patterned wall boundary condition unaffected. Also, $\langle W^0\rangle = W^0$, $\langle W^1\rangle = 0$ and $\langle W^2\rangle$ remain compliant to the boundary condition of $Y = H$ (here no slip). However, errors that decrease exponentially fast with increase of H are incurred at $Y = H$ for the harmonic ($n \neq 0$) parts of the functions W^1 and W^2. It may also be worthwhile to recall here that imposition of boundary conditions on a non-planar boundary such as $Y = \epsilon g(X)$ by any domain perturbation method is only algebraically accurate in ϵ (Van Dyke 1987).

Interestingly, another equivalent, algebraically less cumbersome way of deriving the large-H solution can be perceived. In this method, the exact imposition of the top wall boundary condition can be avoided from the onset of the analysis, except for zero wavenumber terms at each order. Thus, an effective far-field condition can instead be specified (with certain constants for the yet-to-be-determined far field), as follows:

$$\text{As } y \to \infty, \quad W \to \frac{Y}{2} - \frac{Y^2}{2H} + (\epsilon \tilde{C}^{\parallel} + \epsilon^2 C^{\parallel})\left(1 - \frac{Y}{H}\right). \tag{3.10}$$

Equation (3.10) can also be interpreted as a carefully chosen superposition of linear and quadratic shear flows. On further analysis, the constant $\tilde{C}^{\parallel}$ in (3.10) can be evaluated to be zero due to the boundary condition on the patterned wall and the choice of the origin on the mean line, whereas the constant $C^{\parallel}$ comes out as given in (3.9*b*). In contrast to the overall presentation of the current section, the authors could infer the large-H relations, before formally deriving the finite-H relations using the method outlined above. To infer the pattern-averaged streamwise velocity field $\langle W\rangle$ in the large-H regime, the adjusted effective slip length $L_{eff} - \epsilon^2/HS_2$ can be used, where L_{eff} is the effective slip length for the corresponding unbounded (infinite-H) shear flow. The adjustment $-\epsilon^2 S_2/H$ is a consequence of the curvature of the $\langle W\rangle$ field ($\langle W\rangle_{YY} = W_{0YY} \neq 0$ unlike shear flow) and arises from the application of Parseval's identity to the last term on the left-hand side equation (3.5*b*).

On evaluating the flow rate, the final large-H permeability estimate is obtained from

$$\tilde{K}_{\parallel} = (1 - 6\alpha^2 HS_1) + 12\alpha^2 S_2 + e.s.t.(H) + o(\epsilon^2). \tag{3.11}$$

Here and henceforth in the article, the superscript $\sim$ is used to signify the exponentially accurate approximation of the finite channel height effect. The term enclosed by brackets in (3.11) signifies an estimate of permeability based on the expression to the right of the second equality in (3.9*b*), which amounts to also neglecting terms of $C_{\parallel}$ that are algebraically decaying in H. Incidentally, and as discussed later in the article, the expression to the right of the second equality (without the term under the order symbol) in (3.9*b*) also signifies half the effective slip length of the patterned surface in shear flow (Luchini *et al.* 1991).

3.2. *Transverse flow*

The transverse flow is solved conveniently in terms of the streamfunction ψ defined through $U = \partial\psi/\partial Y$ and $V = -\partial\psi/\partial X$. For Stokes flow with a specified pressure drop

between $X=-\pi$ and $X=\pi$ in a channel subject to no slip and no penetration on both the corrugated and planar boundaries of figure 1(*a*), the following need to be observed:

$$\nabla^4\psi = 0, \tag{3.12a}$$

$$\frac{\partial^3\langle\psi\rangle}{\partial Y^3} = -\frac{1}{H}, \tag{3.12b}$$

$$\psi(X, \epsilon g(X)) = 0, \tag{3.12c}$$

$$\psi_Y(X, \epsilon g(X)) = 0, \tag{3.12d}$$

$$\psi_X(X, H) = 0, \tag{3.12e}$$

$$\psi_Y(X, H) = 0. \tag{3.12f}$$

In the following, $\epsilon = 2\pi e/L$ will be treated as a small parameter, and the asymptotic expansions in the form $\psi = \psi^0 + \epsilon\psi^1 + \epsilon^2\psi^2 + o(\epsilon^2)$ together with the method of domain perturbations (Hinch 1991), which involves the transfer the boundary conditions on the curved surface ((3.12*c*) and (3.12*d*)) to $Y=0$ through the Taylor expansion $\psi(X, \epsilon g(X)) = \psi(X, 0) + \epsilon g\psi_Y(X, 0) + \epsilon^2 g^2\psi_{YY}(X, 0)/2 + o(\epsilon^2)$ and a similar expression for $\psi_Y(X, \epsilon g(X))$, will be employed. Here, subscripts denote a derivative. Since the highest-order correction evaluated in this study is ψ^2, all algebraic expressions derived in the current section will contain an $o(\epsilon^2)$ error term. However, for conciseness, this error will not be indicated explicitly in the equations to follow, barring a few exceptions.

3.2.1. *Leading order ($O(1)$)*

The leading-order solution is obtained by setting $\epsilon = 0$ and corresponds to a flat bottom wall at $Y=0$, where the X independent streamfunction ψ^0 is given by

$$\psi^0 = \frac{Y^2}{4} - \frac{Y^3}{6H}. \tag{3.13}$$

3.2.2. *The $O(\epsilon)$ correction*

The first correction ψ^1 is governed by

$$\nabla^4\psi^1 = 0, \tag{3.14a}$$

$$\frac{\partial^3\langle\psi^1\rangle}{\partial Y^3} = 0, \tag{3.14b}$$

$$\psi^1(X, 0) + g(X)\psi^0_Y(X, 0) = 0, \tag{3.14c}$$

$$\psi^1_Y(X, 0) + g(X)\psi^0_{YY}(X, 0) = 0, \tag{3.14d}$$

$$\psi^1_Y(X, H) = 0, \tag{3.14e}$$

which has the solution

$$\psi^1 = \sum_{n\neq 0}^{\infty}(C_{1n}S_n(Y) + D_{1n}T_n(Y))\mathrm{e}^{\mathrm{i}nX}, \tag{3.14f}$$

with constants $\{C_{1n}, D_{1n}\}$ and functions $\{S_n, T_n\}$ as given in appendix A.

3.2.3. *The $O(\epsilon^2)$ correction*

The second correction ψ^2 is governed by

$$\nabla^4\psi^2 = 0, \tag{3.15a}$$

$$\frac{\partial^3\langle\psi^2\rangle}{\partial Y^3} = 0, \tag{3.15b}$$

$$\psi^2(X,0) + g(X)\psi^1_Y(X,0) + \frac{g(X)^2}{2}\psi^0_{YY}(X,0) = 0, \tag{3.15c}$$

$$\psi^2_Y(X,0) + g(X)\psi^1_{YY}(X,0) + \frac{g(X)^2}{2}\psi^0_{YYY}(X,0) = 0, \tag{3.15d}$$

$$\psi^2_Y(X,H) = 0, \tag{3.15e}$$

for which it is sufficient for calculation of the hydraulic permeability to obtain a solution from the pitch-averaged value $\langle\psi\rangle$:

$$\langle\psi^2(Y)\rangle = C^\perp\left(Y - \frac{Y^2}{2H}\right) + D^\perp, \tag{3.15f}$$

where

$$C^\perp = 2\sum_{n=1}^{\infty}(C_{1n}S_n''(0) + D_{1n}T_n''(0))g_n - \frac{1}{H}\sum_{n=1}^{\infty}|g_n|^2, \tag{3.16a}$$

$$D^\perp = -2\sum_{n=1}^{\infty}(C_{1n}S_n'(0) + D_{1n}T_n'(0))g_n - \frac{1}{2}\sum_{n=1}^{\infty}|g_n|^2. \tag{3.16b}$$

Here, superscripts containing $'$ denote differentiation of appropriate order in y.

3.2.4. *Effective permeability*

The effective permeability is obtained by $K = Q(\epsilon, H)/Q(0, H)$. In transverse ($\perp$) flow, $Q^\perp(\epsilon, H)$ is evaluated conveniently from

$$Q^\perp(\epsilon, H) = \langle\psi(X,H)\rangle = \langle\psi^0(X,H)\rangle + \epsilon^2\langle\psi^2(X,H) + o(\epsilon^2)\rangle. \tag{3.17}$$

As in longitudinal flow, we also provide expressions for transverse permeability not only for arbitrary channel height but simpler expressions for a channel height large enough to take advantage of the exponentially decaying part of the effect of H.

For arbitrary channel height. The following $O(\epsilon^2)$-accurate expression for the normalized permeability is obtained with no restrictions on channel height:

$$K^\perp = 1 - 6\alpha^2(HC^\perp - 2D^\perp), \tag{3.18}$$

with $C^\perp$ and $D_\perp$ defined through (3.16*a*) and appendix B. For the special case of $g(x) = \cos(x)$, equation (3.8) reduces to a scaled version of equation (6) of Stroock *et al.* (2002).

Exponentially accurate approximation of the effect of finite channel height. This 'large H' approximation amounts to setting to zero all terms that signify integral powers of

e^{-H} in the preceding expressions, but retaining terms that depend algebraically on $1/H$. For example,

$$C^{\perp} = -2S_1 + \frac{S_2}{H} + e.s.t.(H) = -2S_1 + O(1/H), \tag{3.19a}$$

$$D^{\perp} = -\frac{S_2}{2} + e.s.t.(H). \tag{3.19b}$$

Here, $e.s.t.(H)$ signifies terms that decrease exponentially fast with increase of H. From a spectral viewpoint, these terms are associated at each order with non-zero wavenumbers. Since terms of the above exponential form are needed to impose the top wall no-slip condition on ψ^1 and ψ^2 but not ψ_0, an equivalent way of deriving this approximate solution would be to solve the following specific superposition of quadratic and shear flows with a yet-to-be-determined far field which respects the top wall boundary condition only for the zero wavenumber:

$$\text{As } \mathrm{y} \to \infty, \quad \psi \to \frac{Y^2}{4} - \frac{Y^3}{6H} + (\epsilon\tilde{C}^{\perp} + \epsilon^2 C^{\perp})\left(Y - \frac{Y^2}{2H}\right) + (\epsilon\tilde{D}^{\perp} + \epsilon^2 D^{\perp}). \tag{3.20}$$

The constants $(\tilde{C}^{\perp}, \tilde{D}^{\perp})$ come out to be zero due to the no-slip boundary condition on the curved wall and the choice of the origin on the mean line, whereas $C^{\perp}$ and $D^{\perp}$ come out as given in (3.19). The final expression for the permeability in transverse flow is as follows:

$$\tilde{K}^{\perp} = (1 - 12\alpha^2 H S_1) + 12\alpha^2 S_2 + e.s.t.(H) + o(\epsilon^2). \tag{3.21}$$

Equation (3.21) is the transverse flow counterpart of (3.11) for longitudinal flow. Comparing (3.21) and (3.11), it is clear that, for sufficiently large H, the boundary shape $g(x)$ affects the permeability in either principal direction through the same pair of infinite sums S_1 and S_2 derived from its spectral coefficients g_n.

The term enclosed by brackets in (3.21) signifies an estimate of permeability which amounts to taking an infinitely large H in the expressions for $C_{\perp}$ and $D_{\perp}$ given in (3.16*a*) (or evaluating $C_{\perp}$ and $D_{\perp}$ using the last equality in (3.19)), thus neglecting even terms that decay much slowly (linearly) with increase of $1/H$. To infer the pattern-averaged streamwise velocity $\langle U \rangle$ field in the large-H limit, the adjusted effective slip length $L_{eff} - \epsilon^2 S_2/H$ can be used, where L_{eff} is the effective slip length for the corresponding unbounded (infinite-H) shear flow. The adjustment $-\epsilon^2/HS_2$ is a consequence of the curvature of the $\langle u \rangle$ field ($\langle U \rangle_{YY} = U_{0YY} \neq 0$ unlike shear flow) and arises from application of the Parseval's identity to the last term on the left-hand side of (3.15*d*).

3.3. *Universal relationship between eigenvalues of the permeability tensor*

For isolated surfaces in shear flow represented through the effective slip formalism, a simple algebraic relationship is known to exist between the eigenvalues of the effective slip length tensor (Kamrin *et al.* 2010). It is worthwhile investigating if similar relations exist in confined flow between the eigenvalues of the effective permeability tensor.

Unlike isolated surfaces, the permeability of a patterned surface in both principal (eigen-) directions depends on the channel size (H) in a manner which may at first appear non-trivial to eliminate (e.g. compare equations (3.8) and (3.18) using

respective dependencies) or scale out. However, the situation simplifies considerably when the dependence on H is split into exponentially and algebraically decaying parts, as discussed above. We now derive an interconnecting relationship of comparable simplicity to that applicable between the eigenvalues of the effective slip length tensor (Kamrin *et al.* 2010). This relationship only demands the specification of certain global hydrodynamic and metrological characteristics of the channel and the patterned surface.

Appearance of the sums S_1 and S_2 in both (3.11) and (3.21) allows for the easy elimination of any one of the two, in order to connect the large-H permeabilities $\tilde{K}^{\parallel}$ and $\tilde{K}^{\perp}$. We prefer eliminating S_1 as S_2 has an intrinsic geometrical (and metrological) significance, as discussed below. Thus, the following relationship between the effective permeability calculated in the two mutually perpendicular principal directions of the flow is obtained:

$$2\tilde{K}^{\parallel} - \tilde{K}^{\perp} = 1 + 12\alpha^2 S_2 = 1 + \frac{3\alpha^2}{\pi}\langle g^2 \rangle. \tag{3.22}$$

In the second equality, Parseval's identity has been used to eliminate the Fourier coefficients in favour of the root-mean-squared spatial average $\langle g^2 \rangle$ of the topography. In dimensional terms,

$$2\tilde{k}^{\parallel} - \tilde{k}^{\perp} = \frac{h^2}{12}(1 + 3R_q^2/\pi h^2), \tag{3.23}$$

where R_q is the notation used in the field of surface metrology for root-mean-squared roughness in distance units measured from the mean line (Whitehouse 1994). The equations above indicate that, for sufficiently large channel thickness, a universal relationship completely determined by the variance of the topography exists between $K_{\perp}$ and $K_{\parallel}$ and, therefore, it may be sufficient to know only one of the pair $\{K_{\parallel}, K_{\perp}\}$ to infer the fluid fluxes parallel and perpendicular to any given direction, provided the R_q value of the topography is known from surface metrology (Whitehouse 1994). It can be noted that a similar universal relationship is known to exist among the eigenvalues of the effective slip tensor on isolated surfaces (Kamrin *et al.* 2010; Asmolov & Vinogradova 2012).

Similar relationships can be derived for other flow configurations, such as flow through a channel with applied shear on the walls, free-surface flow, flow with two identical topographic patterns on opposite walls and a combination thereof (see § 3.4). If an otherwise identical pattern is phase shifted on the opposite wall, as may arise in practice due to difficulties in alignment, the effect of phase shift does not appear in the large-H theory, but can be resolved through straightforward but somewhat tedious finite-H-theory calculations following the lines of § 3.

3.4. *Adaptation of asymptotic findings to other flow configurations*

Certain other boundary conditions and flow configurations that arise in practice may be treated by straightforward alterations to the governing equations and boundary conditions. In this section, the normalized permeabilities of certain important configurations will be reported. For example, of relevance to SHS and LIS (Wexler *et al.* 2015; Dubov *et al.* 2018), the boundary condition at $y = H$ can either be (*a*) a prescribed shear with zero applied pressure gradient, or (*b*) a no shear condition under applied pressure gradient, or a combination thereof, as discussed in

Wexler *et al.* (2015) in the context of the shear stability of the lubricants entrapped in the longitudinal grooves of rectangular cross-section in their experiments. For shear flows like (*a*), the dimensional permeability (k) can be defined analogously as before, i.e. the flow rate of a fluid of unit viscosity through the confined passage subject to unit tangential traction at the (solid–fluid or fluid–fluid) interface. The resultant flow for (*a*) will be indicated by the subscript '*s*', standing for shear, and that for (*b*) by subscript '*pzs*', standing for pressure-driven flow with 'zero surface shear'. The resultant normalized permeabilities can then be calculated by steps similar to those described in § 3, differing only in the imposition of the top wall boundary condition. In fact, the expressions for permeability are particularly simple, if in addition, H is large enough to allow the neglect of terms exponentially decaying in H. They are

$$\tilde{K}_s^{||} = 1 - 2\alpha^2(2HS_1 - S_2), \tag{3.24a}$$

$$\tilde{K}_s^{\perp} = 1 - 2\alpha^2(4HS_1 - S_2), \tag{3.24b}$$

$$\tilde{K}_{pzs}^{||} = 1 - 6\alpha^2(HS_1 - S_2), \tag{3.24c}$$

$$\tilde{K}_{pzs}^{\perp} = 1 - 6\alpha^2(2HS_1 - S_2). \tag{3.24d}$$

To address channel height effects completely in longitudinal flow, S_1 in the above expressions can be replaced by the sum $\sum_{n=1}^{\infty} n\tanh(nH)g_n^2$. Corresponding expressions containing finite height effects in transverse flow are placed in appendix B. A selection of the above results can be used to assess the extent of shear-driven drainage of the lubricant entrapped by more general groove shapes than the rectangular shape used in Wexler *et al.* (2015), as discussed later in the article. Owing to the unique scale for velocity used in this study, a shear flow bounded only on one side by the patterned surface can be studied by simply observing the limit $H \to \infty$ in all H-dependent equations reported so far in the article. For such unconfined flows, the pitch-averaged velocity field can be characterized by its effective slip length (L_{eff}), which is the distance between the apparent origin of the flow determined from extrapolation of the far-field velocity (as $Y \to \infty$) to the mean line. The quantity L_{eff} is positive/negative according as the apparent origin lies below/above the mean line. For a no-slip topography L_{eff} is negative.

If the above definition is applied to (3.10) and (3.20) in the limit $H \to \infty$ while setting the constants superscripted with $\sim$ to zero, as discussed in their respective following paragraphs, L_{eff} can be found to be given by

$$L_{eff} = \lim_{H\to\infty} 2C^{||/\perp}\epsilon^2. \tag{3.25}$$

Here, C is given by $C^{||}$ calculated by (3.9*b*) in longitudinal flow and (3.19*a*) in transverse flow. Using (3.9*b*) and (3.19*a*) in (3.25), the relations $L_{eff,||} = -2S_1\epsilon^2$ and $L_{eff,\perp} = -4S_1\epsilon^2$ earlier reported in Luchini *et al.* (1991) and Kamrin *et al.* (2010) are recovered for longitudinal and transverse flows, respectively. In the literature on turbulent drag reduction, a parameter closely related to L_{eff}, named the protrusion height, is also used, which in the current notation will equal $\epsilon + L_{eff}$. More specific details on the above three alternate flow configurations (shear driven, pressure driven with zero surface shear and unconfined shear) are discussed later in the article, along with demonstrations of their practical application to experimentally significant settings from the literature in §§ 4.4 and 4.5. It may be noted here that it follows from symmetry considerations that K_{pzs} is also the normalized permeability of a two-dimensional straight channel with identically patterned walls separated by the distance $2H$.

4. Numerical assessment and applications

Perturbation methods such as in the current study make assumptions on the size of a small parameter (here $\epsilon = 2\pi e/L$). Comparison with solutions from methods which avoid this approximation is therefore useful in quantifying the errors involved in asymptotic approximation, thereby enabling an assessment of the usability of the perturbation method. In this section, after making specific choices for the topographies in § 4.1, comparison with numerical results from a complementary technique, *viz.* finite-element-based fully resolved solutions of the Stokes equation will therefore be made in §§ 4 and 4.3, with an approach for improved numerical accuracy discussed in the latter. Practical applications of the theoretical model will be discussed in §§ 4.4 and 4.5 along with experimental comparisons in the latter. Below, we discuss the motivation as well as rationale for choosing the test topographies defined in § 4.1 for the numerical comparisons in § 4.2.

The degree of smoothness of the topography is an important consideration in applications of the domain perturbation method. The importance on smoothness can be anticipated from a spectral viewpoint, as non-smooth functions have slower decay of Fourier coefficients (Canuto *et al.* 1987) which can in principle cause the sum S_1 of § 3 to diverge, even if a finite variance of the surface profile will ensure that the sum S_2 remains bounded as per Parseval's identity. There are specific studies (Kamrin *et al.* 2010; Asmolov *et al.* 2013*b*), where the domain perturbation method is shown to produce unbounded results when the boundary shape (Kamrin *et al.* 2010) or the degree of boundary slippage (Asmolov *et al.* 2013*b*) is given by certain non-smooth functions. In fact, based on their calculated error bounds, Kamrin *et al.* (2010) mention (p. 417) that it might be incorrect to calculate the effective slip length of an isolated corrugated surface in the form given by (3.25), for 'surfaces with corners and vertical slopes', thus anticipating difficulties with both discontinuous and C^0 smooth functions. An important example of the former is the square-wave topography, where the Fourier coefficients have such a slow decay ($\propto 1/n$) that the infinite sum S_1 in the results of the previous section diverges, rendering effective slip prediction using (3.25) and permeability predictions with (3.11) and (3.21) useless. The difficulty with corners as they appear, e.g. in a triangular-wave topography is less apparent and will be subject to numerical investigations below. Interestingly, for shear flow over discontinuous stick–finite-slip patterns on a planar superhydrophobic surface, where the ratio of the maximum slip length to the pattern pitch is small enough to be employed as a small parameter for asymptotic analysis, Asmolov *et al.* (2013*b*) have shown a divergence of a series similar to S_1 in the coefficient of the second-order term, in case the gauge functions are naively chosen to be powers of the small parameter. Asmolov *et al.* (2013*b*) also present an asymptotic approach that addresses such divergence for discontinuous waveforms. This approach crucially leads to a gauge function of the form $\epsilon^2 \ln(\epsilon)$. However, no such analysis is available for non-planar (corrugated) and wetted no-slip surfaces.

In this section, two test problems are set up with specific wall topography shapes based on the above smoothness consideration. The first topography (labelled Topography A) belongs to the infinitely differentiable or C^∞ class of functions. The second topography (Topography B), which is purposely chosen to be an example with a corner, is a triangular wave. A striking difference between the triangular waveform and the square waveform is the convergence of the sum S_1, which motivated our interest in the former.

In this context, it can be mentioned that the domain perturbation method is also well known to have certain limitations in reproducing local velocity fields, such as

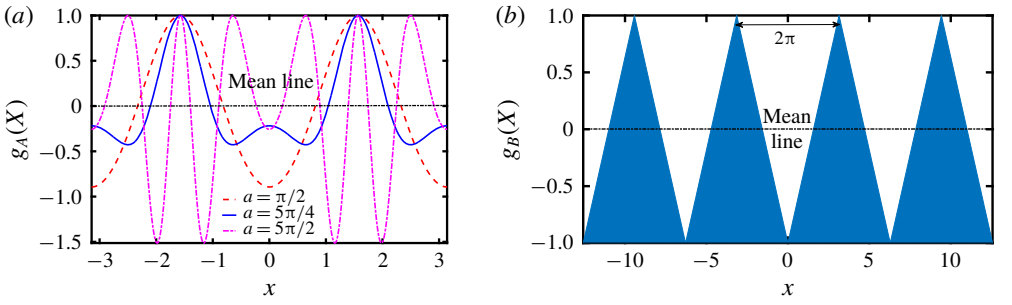

Topography A: Phase modulated sinusoids

Triangle wave for Topography B

FIGURE 2. Surface topography shapes for the two test cases.

inexact imposition of the no-slip condition (Van Dyke 1987). Assessment of the velocity field predictions is therefore not an important concern for the current study. However, for arbitrary periodic topography, our theoretical model reveals another limitation of the domain perturbation method in velocity field prediction, through its spectral decomposition. Depending on the smoothness of the profiles, it is desirable that the expressions for velocity field at various orders must remain bounded (being formed by convergent sums). The Topography B (triangular wave) discussed below actually does not satisfy this criterion for W^1 and U^1; however, our subsequent numerical assessments, perhaps counter-intuitively, reveal that accurate predictions of the permeability (and the effective slip of unbounded surfaces) can nevertheless be obtained for this topography. In this sense, and apprehending the findings of § 4.1, the recommendation of Kamrin *et al.* (2010) based on their error bounds, to avoid the use of the domain perturbation method for predicting the effective slip length of cornered topographies, can be considered to be too stringent.

4.1. *Test problems*

Both the specific topographies to be studied here are normalized to have $\max(g(x)) = 1$, which ensures that the topography is bounded above by $Y = \epsilon$. As a result, when the relative roughness α equals unity, the peak(s) of the topographies will touch the opposing wall. The spectra, sums S_1 and S_2 are evaluated in closed form as far as possible using known results about integral forms and infinite series pertinent to the special functions appearing below (Abramowitz & Stegun 1964).

Topography A: phase-modulated sinusoids. As seen in figure 2(*a*), a family of phase-modulated sinusoids can be parameterized by a dimensionless shape factor a as follows:

$$g^A(X) = \frac{\cos(a\cos X) - J_0(a)}{1 - J_0(a)}. \tag{4.1}$$

Note that a base shift has been applied to the basic phase-modulated cosine function $\cos(a\cos X)$ to ensure $\langle g \rangle = 0$. In addition, the denominator provides a scale shift that ensures that the peak value of g_A does not exceed unity, so that the value of ϵ is indeed representative of the characteristic pattern size. Equation (4.1) exemplifies a reasonably complex but smooth topography which can have a number of local and global extrema tuneable with the parameter a. The three a values shown are $a = \pi/2, 5\pi/4, 5\pi/2$. For $a = 5\pi/4$, eight extrema (four global minima, two local

maxima and two global maxima) and four zero crossings occur over one wavelength of topography, although the variance of 0.225 for $g^A(X)$ with $a = 5\pi/4$ (as calculated from (4.2*c*) using Parseval's identity) is the lowest of the three profiles shown. For $a = 5\pi/2$, twelve extrema (six global maxima, four global minima, two additional local minima) and twelve zero crossings occur per pattern pitch, and the variance is also the largest (0.49). The relatively less complex (in terms of types and number extrema) profile for $a = \pi/2$ has four extrema (two maxima and minima) with four zero crossings but the second highest variance of 0.449 among the three a values shown. The asymptotic variance for large a calculated from (4.2*c*) is 1/2, but is reached through very slow oscillations. Although, a phase-modulated sinusoid in time is an important waveform in signal processing and optics (Dunlop 2017), we are unaware of any study utilizing its spatial version in the study of fluid flow phenomena. The Fourier coefficients of Topography A are available in closed form, thanks to Jacobi–Anger expansions (Abramowitz & Stegun 1964). Topography A can be represented by

$$g^A(X) = \sum_{n=-\infty}^{\infty} g_n^A \mathrm{e}^{\mathrm{i}nX}, \tag{4.2a}$$

$$g_n^A = \begin{cases} (-1)^{n/2} J_n(a), & \text{if } n \text{ is an even integer,} \\ 0, & \text{otherwise,} \end{cases} \tag{4.2b}$$

$$S_2^A = \sum_{n=1}^{\infty} |g_n^A|^2 = \frac{1}{4} \frac{(J_0(2a) - 2J_0^2(a) + 1)}{(1 - J_0(a))^2}. \tag{4.2c}$$

A closed-form expression for $S_1^A = \sum_{n=1}^{\infty} |n g_n^A|^2$ appears not to be available, although p. 532 of Watson (1995) equates this sum to an iterated integral. It was found to be convenient to approximate S_1^A to at least four-digit accuracy numerically by truncation to a sufficiently large number of terms.

Topography B: triangular grooves. The triangular-wave topography (figure 2*b*) which is represented by the wall shape given by (4.3*a*), and on which periodicity is imposed by (4.3*b*), is a non-smooth topography possessing 'corners'. The permeability for this topography has a spatial and spectral description that allows the convenience of closed forms, as revealed by the following results:

$$g^B(x) = 2\frac{|X|}{\pi} - 1 \quad \text{in } -\pi \leqslant x \leqslant \pi, \tag{4.3a}$$

$$g^B(X + 2\pi) = g^B(X), \tag{4.3b}$$

$$g^B(X) = \sum_{n=-\infty}^{\infty} g_n^B \mathrm{e}^{\mathrm{i}nX}, \tag{4.3c}$$

$$g_n^B = \frac{2(-1 + (-1)^n)}{n^2\pi^2}, \tag{4.3d}$$

$$S_1^B = \sum_{n=1}^{\infty} n|g_n^B|^2 = \frac{14}{\pi^4}\zeta(3), \tag{4.3e}$$

$$S_2^B = \sum_{n=1}^{\infty} |g_n^B|^2 = \frac{1}{6}. \tag{4.3f}$$

The closed forms given by (4.3*e*) and (4.3*f*) for the sums required for the large-H exponentially accurate calculation of the normalized hydraulic permeability of the triangular-grooved surface are obtained using the properties of Riemann zeta functions (Abramowitz & Stegun 1964), leading to

$$\tilde{K}_{\parallel}^{B} = 1 - \frac{12\alpha^2}{\pi^4}\left(7H\zeta(3) - \frac{\pi^4}{6}\right), \tag{4.4a}$$

$$\tilde{K}_{\perp}^{B} = 1 - \frac{12\alpha^2}{\pi^4}\left(14H\zeta(3) - \frac{\pi^4}{6}\right). \tag{4.4b}$$

Here, ζ stands for the Riemann zeta function for which precise enumeration/tabulation and numerical implementations are readily available and $\zeta(3) = 1.20205\cdots$ is also known as Apéry's constant (Sloane 2019). Equation (4.4*b*) is an important closed-form result from this study applicable for the friction factors of the oft-studied triangular topography (Taylor 1971; Dey, Saha & Chakraborty 2018).

4.2. *Numerical assessment of analytical results*

The expressions for permeability provided in § 3 are expected to be accurate only for sufficiently small values of ϵ. For numerical assessment of the errors arising from the asymptotic approximation, a finite-element-method-based solution of the governing equations and boundary conditions discussed in § 3 is obtained using the commercial software COMSOL Multiphysics© (COMSOL AB, Sweden). The permeability values are calculated on the basis of the numerically calculated flow rate. Independence of the calculated permeability values from the sizes of the unstructured triangular mesh used in the simulation is tested for the largest reported ϵ ($\epsilon = 5$) and for $\alpha = 0.99$ (99 % channel blockage in transverse flow) up to four-digit accuracy. In transverse flow, mass conservation was ensured between the three cross-sections at $x = -\pi, 0, \pi$ up to at least four-digit accuracy, and the flow rate through the $x = 0$ plane is used for permeability evaluation. Any infinite sums required by the theoretical model, for which a closed form is not reported in this article, are evaluated by numerical truncation to at least four-digit accuracy.

In figures 3–5 the asymptotic predictions for permeability are compared against the corresponding numerical predictions for a range of ϵ values. The range of ϵ shown in the abscissae of this figures correspond to either $<5\,\%$ error committed relative to the numerical predictions by the arbitrary-H theory, or the pattern peaks touching the opposite wall ($\alpha = 1$), depending on which of these two limits is reached at a smaller ϵ. The latter situation occurs only for figures 4(*a*) and 5(*a*). Based on the above definition, the largest value of ϵ appearing in all other figures will be designated as $\epsilon_{max}^{5\,\%}$.

In figures 3–5, whenever the arbitrary H prediction (shown as solid black lines) is indistinguishable up to four-digit accuracy from the exponentially accurate large H predictions, which have simpler analytical forms, only the latter (blue dashed curves) is shown. Also, shown as dotted curves, whenever numerically comparable predictions are obtained, are the approximations obtained from removing even the algebraically H-decaying terms, i.e. using only the bracketed terms of (3.11) and (3.21) to estimate the permeability. A dotted curve thus signifies the best permeability prediction that can be obtained by using only the existing domain-perturbation-based theoretical models (Luchini *et al.* 1991; Kamrin *et al.* 2010) for arbitrary periodic surface topographies, which are all limited to shear flows. It is clear that, in none

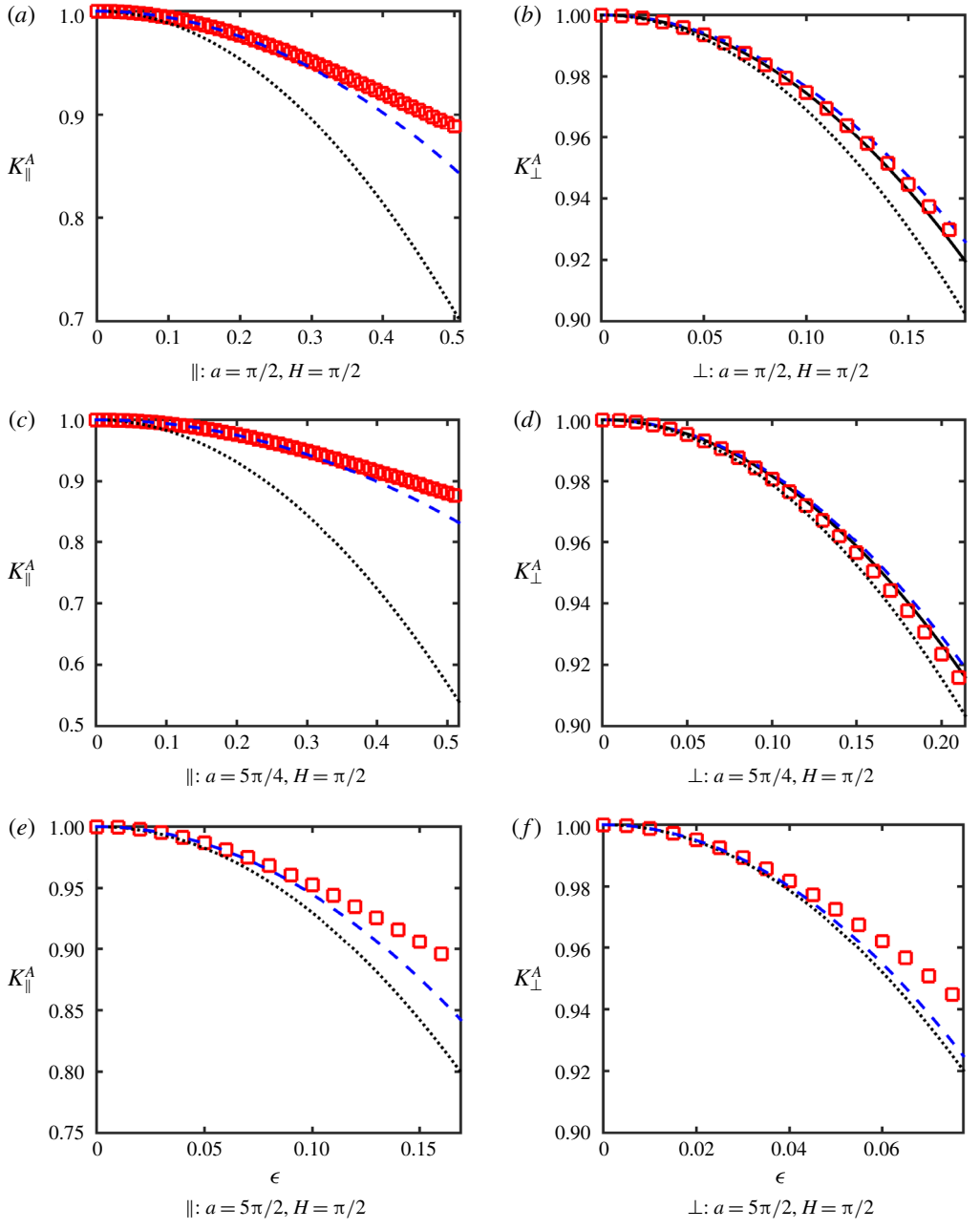

FIGURE 3. Variation of effective permeability with dimensionless characteristic pattern size (ϵ) in longitudinal (*a*,*c*,*e*) and transverse flow (*b*,*d*,*f*) for different values of a and $H = \pi/2$ in Topography A. The solid black line, blue dashed line and black dotted line indicate the asymptotic predictions from finite channel height theory (3.8)/(3.18), exponentially accurate theory for the finite channel height effect (3.11), (3.21) and $O(1/H)$ theory (only the bracketed terms of (3.11), (3.21)). The red square symbols are data from fully resolved numerical simulations employing the finite-element method. The range of ϵ values shown in each figure corresponds to $<5\,\%$ numerical error by the finite height theory.

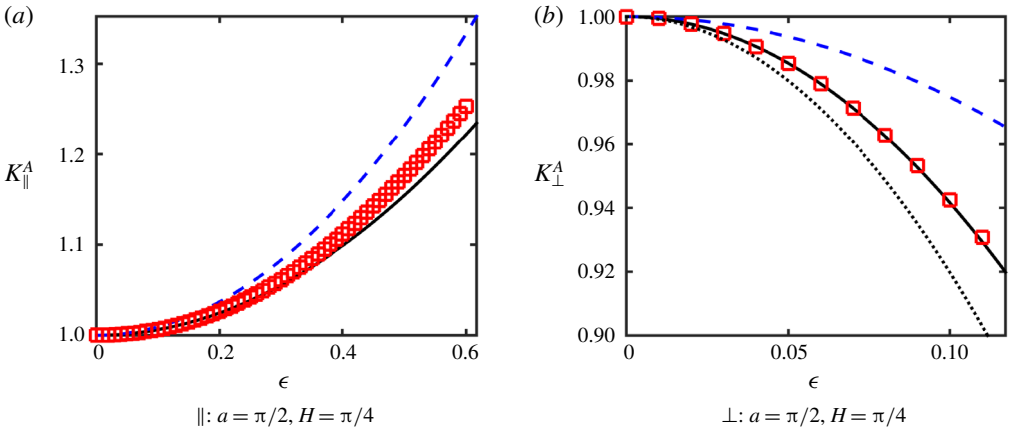

FIGURE 4. Variation of effective permeability with dimensionless characteristic pattern size (ϵ) in longitudinal (a) and transverse flow (b) for $a = \pi/2$ and $H = \pi/4$ in Topography A, as predicted by fully resolved simulations (symbols) and asymptotic theories. The colour/pattern of lines with respect to different asymptotic theories have the same meaning as in figure 3. The range of ϵ values shown in each panel corresponds to $<5\,\%$ numerical error by the finite height theory. The peaks of the pattern touch the planar top wall ($\alpha = 1$) at the rightmost value of abscissa in (a).

of figures 3–5, can the shear-flow model be applied at levels of accuracy comparable to the large-H and finite-H models, although its performance is superior in transverse flow. This can be rationalized from the algebraic decay of errors in the expressions to the right of the second equal sign in (3.9*b*) and (3.19*a*). The shear-flow model is therefore excluded from subsequent discussions, although it is shown in the figures. Lubrication theory predictions of K (not shown) for thin channels which equal the arithmetic and harmonic means over one period of the function of $(1 + \alpha g)^3$ in longitudinal and transverse directions, respectively, were found to be exceedingly inaccurate even for the smallest H studied in figures 3–5, and are therefore kept out of consideration. The numerical errors (not shown) were monotonic with ϵ for all situations studied in figures 3–5.

Figures 3 and 4 pertain to wall Topography A and show the effect of parameter a and channel size H, respectively. Figure 5 shows the effect of channel size H with wall Topography B. While for sufficiently small ϵ the asymptotic theories are expectedly accurate, qualitatively different patterns emerge in the behaviour of both the permeability and the error of the asymptotic prediction, depending on the functional form of the topography and the orientation of the topography with respect to the mean flow.

For longitudinal flow, $\epsilon_{max}^{5\,\%}$ increases with miniaturization (decreasing the dimensionless nominal channel size H) for both topographies. For transverse flow, the corresponding ϵ_{max} decreases with miniaturization for both the topographies. The latter behaviour can be expected since, in transverse flow, a decrease of H implies the creation of more significant blockages in the flow passage, and as ϵ approaches H ($\alpha \to 1$) the flow passage is completely blocked.

Figure 3 along with figure 2(*a*) suggest that more complex Topography A shapes (with a larger number of extrema) have a steeper drop in the numerically calculated permeability values with ϵ and also pose a stronger challenge to asymptotic theories in

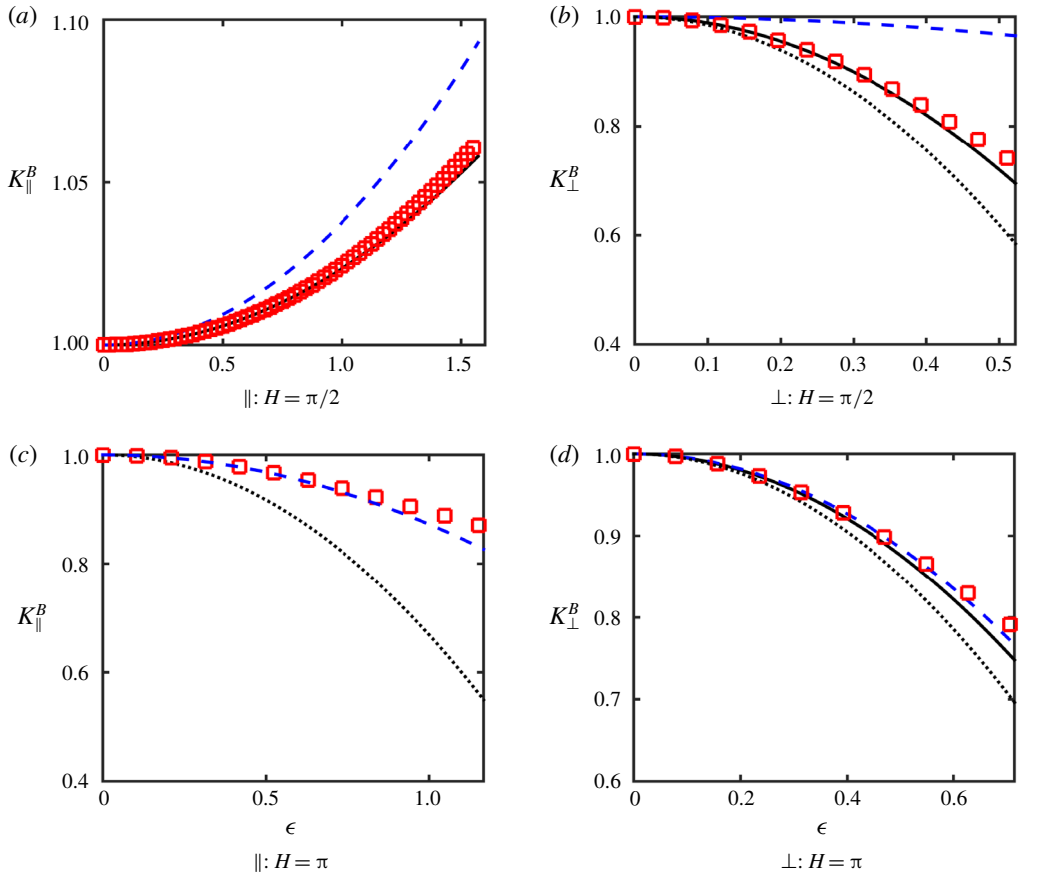

FIGURE 5. Variation of effective permeability with dimensionless characteristic pattern size (ϵ) in longitudinal (*a*,*c*) and transverse flow (*b*,*d*) for different values of H in Topography B, as predicted by fully resolved simulations (symbols) and asymptotic theories. The colour/pattern of lines with respect to different asymptotic theories have the same meaning as in figure 3. The range of ϵ values shown in each figure corresponds to $<5\,\%$ numerical error by the finite height theory, except for $H = \pi/2$ (*a*) in longitudinal flow, where the numerical error is $<1.67\,\%$ up to the rightmost value of the abscissa where the peaks of the pattern touch the planar top wall ($\alpha = 1$).

the sense that $\epsilon_{max}^{5\,\%}$ is smaller for $a = 5\pi/2$ than $a = 5\pi/4$. Qualitatively, this finding may be attributed to the appearance of strong velocity gradients not amenable to asymptotic treatment. Strong gradients can be expected from both the larger variance (0.49 versus 0.225 for $a = 5\pi/4$) as well as the more complex shape of the $a = 5\pi/2$ topography (figure 7*c*). The narrow wall-proximal gorges for $a = 5\pi/2$ create large gradients in longitudinal flow; in transverse flow the tortuous path of near wall fluid particles is also a reason for the appearance of large gradients. The larger variance of the topography with $a = 5\pi/2$ also signifies a larger distance between peaks and troughs and a larger 'sidewall' perimeter of liquid–solid contact per pitch. Despite its relatively simple shape, the topography with $a = \pi/2$ has nearly twice the variance (0.449) of the topography with $a = 5\pi/4$ (0.225). The $\epsilon_{max}^{5\,\%}$ values for $a = \pi/2$ and $a = 5\pi/4$ are broadly of comparable magnitude, regardless of the flow orientation.

This finding can be interpreted in terms of an interplay between the comparable simplicity in shape of the $a = \pi/2$ and its larger variance. The former is expected to make the asymptotic approximations accurate, while the latter is expected to disrupt the accuracy.

To understand the role of the shape of the topography, two distinct forms of Topography A were chosen with the variance controlled strictly to its asymptotic value $1/2$. The a values of these topographies can be obtained by numerically finding the roots of (4.2*c*) with the right-hand side set to $1/2$. The two smallest roots are $a = \{a_1, a_2\}$ with $a_1 = 5.68$ and $a_2 = 8.12$. It was found that a stronger ϵ-dependence of the numerically calculated permeability as well as a larger degree of inaccuracy (as estimated by $\epsilon_{max}^{5\,\%}$) in asymptotic prediction occurred for the more complex topography ($a_2 = 8.12$). Thus, in addition to the role of the root-mean-square (r.m.s.) height (or variance), the specific a-dependent shape of 'Topography A' plays an important and independent role in determining the degree of (in)accuracy of the asymptotic predictions. The 'complexity' of the a-dependent shape reflects in the number of zero crossings, depth, width and number of gorges and hills. For a more 'complex' shape obtained with a larger a, the asymptotic theory has the prescribed numerical accuracy of 5 % up to a smaller ϵ value in comparison to that for a shape with smaller a, even when both have the same R_q roughness.

There are observable distinctions between longitudinal and transverse flows across all topographies. At H is lowered progressively, the large-H trend of permeability decreasing with pattern amplitude (ϵ) transitions into an increase with ϵ in longitudinal flow, whereas the trend of decrease of permeability with ϵ occurs at all H in transverse flow. In general, the asymptotic approaches are more accurate for longitudinal flow than transverse flow. Further, the numerical accuracy of the predictions worsens with decreasing channel size in transverse flow, while the accuracy improves in longitudinal flow on reducing the channel size. In transverse flow, the asymptotic theory obviously encounters more difficulties as it has to cope with a stronger decrease of permeability with ϵ, as signified by the complete flow blockage at $\epsilon = H$. If H is small enough, contact with the top wall ($\alpha = 1$) poses no significant challenge to numerical accuracy of the arbitrary-H theory in longitudinal flow, e.g. the error is $<1.67\,\%$ for a triangular wave at $H = \pi/2$ (figure 5*a*) and $<5\,\%$ for the phase-modulated cosine at $H = \pi/4$ (figure 4*a*). This observation will be useful in studying an application of the theory to the shear stability of lubricant-infused textured surfaces later in the article.

Between the two topographies, comparison of height effects in figures 3 and 4 reveals that, in the smoother topography (Topography A), the onset of the large-H behaviour occurs at a smaller height, whereas the cornered peaks of a triangular pattern (Topography B) exert their influence up to larger distances, requiring larger H values for a reasonable accuracy from the large-H theory in comparison to the smoother Topography A.

Figure 5 provides verification that the presence of corners in the triangular profile does not preclude the asymptotic theory from providing numerically accurate permeability predictions for a triangular profile for sufficiently small ϵ values. As per the steps of our theoretical model shown in § 3, correct effective permeability prediction necessarily requires correct effective slip prediction. The findings in figure 5 therefore contradict the directive of Kamrin *et al.* (2010) on the avoidance of 'surfaces with corners' in using domain perturbation for prediction of effective slip, as discussed at the beginning of current section. This finding can be anticipated theoretically from the convergence of S_1, as it follows that $S_1 \propto L_{eff}$, when L_{eff} is calculated either by (5.1) of Kamrin *et al.* (2010) or equation (3.25). The latter can be recalled to be obtained in the limit $H \to \infty$ of the current theoretical model.

Interestingly, the effective permeability with the triangular profile is accurately predicted, despite the fact that the series in certain intermediate results pertaining to the local flow field such as W^1 from (3.4*a*) and U^1 from (3.14*f*) (up to *e.s.t.*(H)) are actually divergent.

Another consequence of the smoothness of the test topographies is corroborated by the numerical comparisons. If the sums required for the expression for permeability are truncated to the same number of (sufficiently large) modes, the predictions for C^∞ smooth Topography A was found to provide higher numerical accuracy than those for C^0 smooth Topography B, which can be anticipated from the faster convergence gained from the faster asymptotic decay of the Fourier coefficients (Canuto *et al.* 1987) of Topography A.

4.3. *Extension of the range of accuracy of the asymptotic approximations*

For the usability of asymptotic approximations, 'how large an ϵ' can be admitted by a nominally small-ϵ theory is an important question (Dyke 1984; Dewangan & Datta 2019). Polynomial form approximations (even with higher orders) do not often provide numerically encouraging answers to this question, which can be attributed to convergence limitations imposed by the singularities in the complex ϵ-plane possessed by the functions these polynomials expand in Taylor series. Although obtaining an extended accuracy solution requires a knowledge of a sufficiently large number of terms of the polynomial which cannot be afforded here, we note that for any $a + b\epsilon^2 + o(\epsilon^2)$-form prediction in this article, an alternative form avoiding polynomials and attempting to anticipate singularities can be heuristically chosen as the asymptotically equivalent (1, 2) Padè (rational) approximant form $a^2/(a - b\epsilon^2) + o(\epsilon^2)$. In the typical situation, except for small H, where the permeability decreases with ϵ, there is also a large-ϵ tendency in the numerically evaluated scaled permeability value to saturate, which is broadly consistent with the infinite groove depth effective slip predictions from the literature obtained by the Wiener–Hopf method (Hocking 1976; Luchini *et al.* 1991). This behaviour can be anticipated to be captured better by a rational approximant due to the presence of a denominator. Thus, the rational approximations accessible to the current theoretical model were subject to numerical experimentation.

Figure 6 for triangular grooves with $H = 2\pi$ in transverse flow over Topography B is an example of extending the ϵ-range of validity using rational approximations, where approximately 50 % lower permeability values (from $\sim$0.8 to $\sim$0.4) or permeability at nearly three times larger ϵ (up to $\epsilon \simeq 5$) can be predicted with 5 % accuracy using the Padè approximant corresponding to the two-term polynomial approximation given by (3.18). The polynomial approximation produces unphysical negative results at $\epsilon \simeq 5$ where the Padè approximant reaches five per cent error. Qualitatively similar improvements were offered by the Padè approximant for both the topographies, whenever permeability decreased with ϵ in either longitudinal or transverse flow. For permeability increasing with ϵ where there is no saturation effect at large ϵ, polynomial (here parabolic) approximation was expectedly (although marginally) superior until $\alpha = 1$ is reached.

4.4. *Application to slippery lubricant impregnated surfaces*

Biologically inspired patterned surfaces infused with a lubricant (LIS) have gained attention for a diversity of applications for their much-desirable liquid repellency, self-cleaning, self-healing, anti-icing, dropwise-condensation-promoting properties

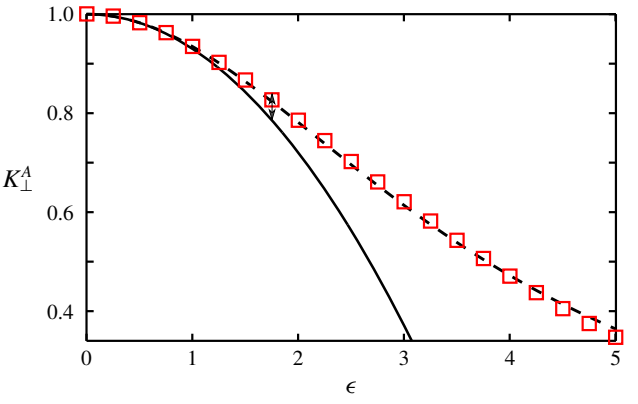

FIGURE 6. Demonstration of range extension through use of the (1, 2) Padè approximant (dashed lines) and polynomial form (solid lines) of the asymptotic predictions for triangular grooves with $H = 2\pi$. The symbols are from fully resolved simulations. The range of ϵ values shown corresponds to $<5\,\%$ numerical error by the Padè (1, 2) approximant. The double arrow indicates the location where 5 % error is incurred by the polynomial form approximation.

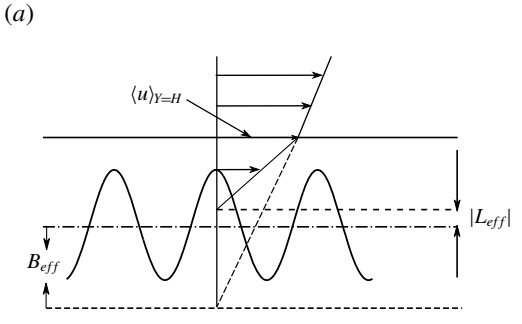

The 'Lubricant' cushion model for LIS/SHS

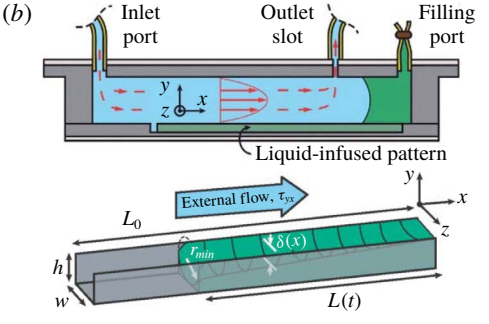

Experimental configuration of Wexler *et al.* (2015)

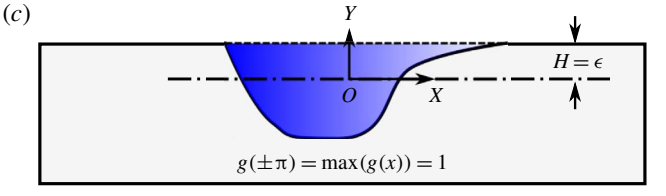

A complex groove shape

FIGURE 7. (*a*) Shows a schematic of a pitch-averaged gas/lubricant cushion model of effective slip for hydrodynamic characteristics of LIS/SHS. (*b*) Is an adapted reproduction of figures 1(*a*) and 2(*c*) of Wexler *et al.* (2015) showing their flow cell (above) and the rectangular groove containing the lubricant (below). (*c*) Is the cross-section of a conceived complex-shaped lubricant groove under experimental conditions otherwise identical to Wexler *et al.* (2015). In (*a*), the stripes are transverse to the period-averaged velocity $\langle U \rangle$. Panel (*b*) is reproduced from Wexler *et al.* (2015) with permission from the American Physical Society.

(Wong *et al.* 2011), in addition to a possible capability to reduce drag (Solomon *et al.* 2018). Two distinct applications of the developed theory to LIS will be discussed. Capacity to represent the role of a complex texture analytically is a connecting feature of the applications. For simplified modelling of these multi-phase systems, a simplification used here will involve giving prescribed shapes to fluid–fluid interfaces, which helps us maintain analytical tractability. In principle, more-resolved multi-phase model(s) of flows over LIS may, however, be constructed numerically or in the long-wave limit (Qi & Ng 2015; Sun & Ng 2017).

Roughness effects on the lubricant cushion model. Consider a submerged complex topography underneath the interface between a lubricant (with viscosity μ_2) and the working fluid (with viscosity μ_1) as shown in figure 7(*a*). Here, a procedure to incorporate the effects of the topography into the pitch-averaged velocity field of the working fluid will be shown, based on the gas/lubricant cushion model (Nizkaya *et al.* 2015; Dubov *et al.* 2018). In principle, the interface may touch the peaks of the topography in figure 7(*a*) without invalidating the subsequent description. The macroscale (period-averaged) construction for the gas/lubricant cushion model (Vinogradova & Belyaev 2011; Nizkaya *et al.* 2015; Dubov *et al.* 2018) for the effective slip length B_{eff} of the LIS referred to the mean line of the topography is shown in figure 7(*a*), assuming a case favourable for drag reduction ($\mu_1/\mu_2 > 1$). In figure 7(*a*), stripes are transverse to the period-averaged velocity $\langle U \rangle$ although in principle the tensorial slip length (Bazant & Vinogradova 2008) formalism can be used to generalize this description. Note that B_{eff} must be distinguished clearly from L_{eff}. The latter gives the location of the effective no-slip plane for the submerged topography with respect to the mean line. The magnitude of the negative-signed L_{eff} is shown in figure 7(*a*). As per the construction of the 'gas/lubricant cushion model' shown in figure 7(*a*), the continuity of stress and the fact that the effective no-slip plane is shifted upward by a distance L_{eff} due to the complex topography allows us the following adaptation of the traditional 'gas cushion model' to calculate the scaled effective slip length B_{eff}:

$$B_{eff} = \left(\frac{\mu_1}{\mu_2} - 1\right) H - \frac{\mu_1}{\mu_2}|L_{eff}|. \tag{4.5}$$

Equation (3.25) of the current work can provide the L_{eff} required in (4.5), thus allowing the effect of topographies encapsulated by the lubricant to be evaluated under a gas-cushion model-based effective slip formalism. It can be noted, however, approaches to improving the local resolution of the traditional gas cushion model employed here has been proposed, which require specification of a distribution of the slip length over the gas–liquid interface (Dubov *et al.* 2018).

In figure 7(*a*), a provision is maintained for a film of liquid overlying the tips of the topography, which has been found experimentally to be desirable for drag reduction (Solomon *et al.* 2018), but not necessarily for shear stability of the lubricating fluid (Wexler *et al.* 2015).

Shear stability of lubricant entrapped by complex groove shapes. Stability under shear is a perceived weakness of lubricant-infused patterned surfaces that needs to be addressed, if they are to be used in dynamic fluid environments, e.g. for antibacterial/anti-fouling protection in the human circulatory system or on marine surfaces. The next application is inspired by the study of shear stability of lubricant fluid in patterned surfaces with infused lubricants conducted by Wexler *et al.* (2015).

In this study, for the experimental configuration of longitudinal flow ('worst-case scenario' for shear stability, to quote the authors) shown in figure 7(*b*), it is demonstrated that the lubricant (in the regime $\mu_1/\mu_2 \ll 1$) combats the drainage effects of shear τ_{xy} from the overlying fluid through a pressure-driven back flow arising from the Laplace pressure at the interface with surface tension γ as a result of which an equilibrium length L_∞ of the lubricant is always adherent. According to Wexler *et al.* (2015), the larger the value of L_∞ the more shear stable is the surface. Equation (2) of Wexler *et al.* (2015) provides an equation for L_∞ applicable to rectangular grooves. If the derivation of equation (2) as discussed in section 2 of the supplementary material for Wexler *et al.* (2015) is retraced, an essential component of their model involves evaluating the permeability for the fully developed combined shear and back pressure driven flow in a channel of rectangular cross-section. From § 3.4 of the current study, the permeability of the component longitudinal shear-driven (*s*) and free-surface pressure-driven (*pzs*) flows can be evaluated for more general shapes, using the finite-H generalization of (3.24*b*) and (3.24*c*) which, as discussed earlier, involves replacing the sum S_1 appearing in this equation by $\sum_{n=1}^{\infty} n\coth(n)g_n^2$.

Given the generality of certain results (specifically the finite-H versions of (3.24*b*) and (3.24*c*) from § 3.4) of this study on longitudinal shear-driven (*s*) and free-surface pressure-driven (*pzs*) flows, in this section we outline the procedure to generalize their result to groove shapes that are more complex than rectangular.

A plausible situation where more complex topographical patterns given by a function $g(x)$ are used to contain the lubricant can be envisaged as shown on figure 7(*c*), where the lubricant film thickness measured from the mean line is given by H. The physical requirement of pinning the interface to the tips of the topography (encapsulation being considered undesirable for shear stability) and the geometrical requirement of the side 'walls' in addition to the bottom 'wall' of a complete 'groove' being formed by specifying the single function $g(x)$ together with the need for 2π-periodic extension enforce the following restrictions on the groove shape and size: $\alpha = 1$ (or $\epsilon = H$) and $g(\pm\pi) = \max(g(x)) = 1$. It is assumed here that $g(X)$ is so scaled that $\alpha = 1$ corresponds to tips touching the interface. These restrictions are also indicated in figure 7(*c*).

For such a groove, otherwise retracing the derivation of equation (2) of Wexler *et al.* (2015) leads to the following proposed generalization with the new definitions written in the notation of the current work:

$$L_\infty = \frac{2A}{3}\frac{K_{pzs\|}}{K_{s\|}}. \tag{4.6}$$

Recollecting Wexler *et al.* (2015), the constant of proportionality is $A = (h\gamma)/(\tau_{yx}r_{min})$, where r_{min} is the minimum transverse radius of curvature on the upstream edge of the lubricant layer (shown for rectangular grooves in figure 7*b*). If the quantity $K_{pzs\|}/K_{s\|}$ is evaluated using (3.24*b*) and (3.24*c*), it may be inferred that a complex groove topography with a large R_q measure (leading to larger S_1) for the 'roughness' appears to be desirable for increasing L_∞, which in turn offers improved shear stability.

It should be noted, however, that numerical comparisons in § 4 have indicated that the small $-\epsilon$ theory underlying the permeability predictions is numerically accurate even at $\alpha = 1$ for sufficiently shallow (small-H) grooves. For example, for $H = \pi/2$, the triangular grooves in figure 5(*a*), the accuracy at $\alpha = 1$ is 1.67 %. Incidentally, the value of H for the rectangular-wave topography fabricated by Wexler *et al.* (2015), which is shown in panel (*d*) of figure 1 of their study, is approximately 2.8 using

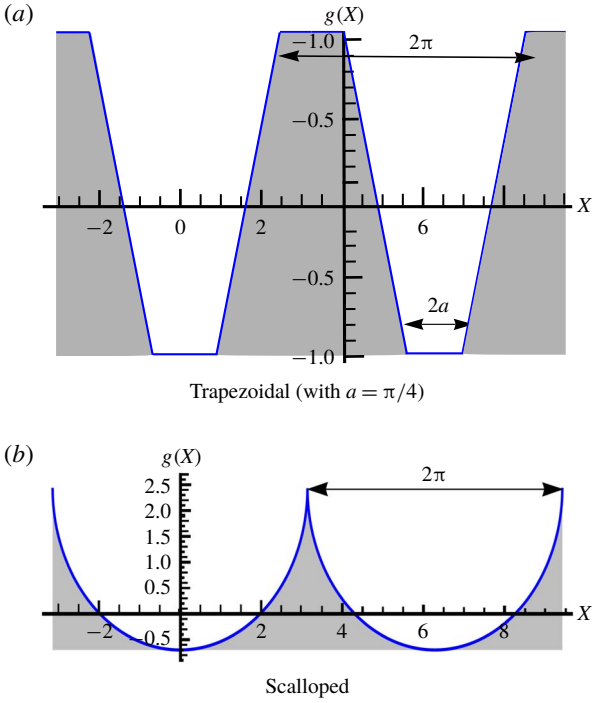

FIGURE 8. Trapezoidal and scalloped topographies. The function $g(x)$ is shown by blue lines, which overlie the grey-shaded solid zone.

the data provided in that work. It is worthwhile, however, to recall that the domain perturbation approach, despite its applicability to complex groove shapes similar to that shown in figure 7(*c*), does not specialize meaningfully to the rectangular topography, because of its jump discontinuity (Kamrin *et al.* 2010).

4.5. *Other surface topographies and experimental comparison*

In this section, we study certain distinctive topographies arising in applications and perform a comparison with experimental data from the literature. The closed-form results presented here are obtained using known results on the infinite series pertinent to the special functions appearing below (Abramowitz & Stegun 1964).

Topographies presenting a cusp have attracted the attention of several researchers (Richardson 1973; Bechert & Bartenwerfer 1989), partly because of their importance in the design of turbulent-drag-reduction riblets. Geometrically, and in terms of local flow resolution, cusps are interesting in comparison to corners (such as in Topography B) as the left- and right-side derivatives are not finite. The scalloped pattern obtained by joining semicircles shown in figure 8(*b*) is in fact a common motif in engineering and biology (Imani & Elbestawi 2001; McCarthy, Ring & Rana 2010). The current spectral approach is very convenient to access the oft-used semicircle-based scalloped pattern, as shown through the evaluation of the parameters for closed-form large-H permeability prediction in the second row of table 1. Unlike the current study, the cusped patterns obtained through conformal-mapping approaches in the literature (Richardson 1973; Bechert & Bartenwerfer 1989) involve approximations to the semi-circle, necessitated by the specific mapping functions.

Pattern	$g_n(n \neq 0)$	S_1	S_2
Trapezoidal	$\dfrac{[-1+(-1)^n]\cos an}{\pi^2 n^2\left(1-2\dfrac{a}{\pi}\right)}$	Equation (4.7)	$\dfrac{1}{6}+\dfrac{2a}{3\pi}$
Scalloped	$\dfrac{\pi J_1(n\pi)}{2n}$	$0.3498\cdots$	$\dfrac{\pi^2}{3}-\dfrac{\pi^4}{32}$

TABLE 1. The Fourier coefficients and sums required for large-H permeability evaluation with trapezoidal and scalloped topographies shown in figure 8. The parameter $a < \pi/2$ for the trapezoidal profile.

Converged predictions are provided by the current theory even for cusped profiles (but not for profiles with jumps). The results of table 1 concerning the trapezoidal and scalloped topographies shown in figure 8 are in closed form, except the numerically summed S_1 for the scalloped profile. The asymptotic validity of the permeability predictions from table 1 were also numerically tested against finite-element predictions, although not shown here for brevity.

The first row of table 1 presents parameters for trapezoidal grooves parameterized by the distance a (figure 8*a*). Lecoq *et al.* (2004) have performed experiments on the effect of trapezoidal wall corrugations on the drag on an approaching sphere, while Bechert & Bartenwerfer (1989) have studied the protrusion length of trapezoidal grooves in shear flow through conformal mapping. Trapezoidal grooves often arise as inevitable consequences of fabrication and machining processes (Rangsten *et al.* 1998; Lecoq *et al.* 2004), even when square ($a = \pi/2$) or triangular grooves ($a = 0$) are targeted. For the domain perturbation approach to give bounded permeability predictions, the value of a must be restricted in the trapezoidal surface profile to $0 \leqslant a < \pi/2$, again due to its non-resolution of jump discontinuities (Kamrin *et al.* 2010).

We have evaluated the sum S_1 required for the trapezoidal grooves shown in figure 8(*a*) analytically, including an asymptotic form avoiding special functions. The sum S_1 is given by

$$\begin{aligned} S_1 &= \frac{7\zeta(3)+8\mathrm{Re}(\mathrm{Li}_3(\mathrm{e}^{2\mathrm{i}a})-\frac{1}{8}\mathrm{Li}_3(\mathrm{e}^{4\mathrm{i}a}))}{\pi^2(\pi-2a)^2} \\ &= -\frac{14\zeta(3)+8a^2\log(a)-\dfrac{100a^2(907a^2-5292)}{67a^4+5925a^2-44\,100}+O(a^{10})}{\pi^2(\pi-2a)^2}. \end{aligned} \tag{4.7}$$

In the above, Li is the polylogarithm function. The second equality obtained with Padè approximants, although nominally valid for small a, gives $<1\,\%$ error for $0 \leqslant a < 1.355$, i.e. over $86\,\%$ of the domain of definition $0 \leqslant a < \pi/2$.

Lecoq *et al.* (2004) have performed experiments inquiring about the location of the effective no-slip plane when a sphere approaches a precisely fabricated corrugated surface. More recent experiments with a similar configuration are available (Mongruel *et al.* 2013), but for rectangular grooves, the domain perturbation approach of the current model fails to give a bounded prediction, as discussed elsewhere in the article and the literature (Kamrin *et al.* 2010; Asmolov *et al.* 2013*b*). Although the current study mainly concerns confined flows, the location of the effective

no-slip plane is a by-product of the current study, as per (3.25). The experimental amplitude to pitch ratios of the trapezoidal corrugations used in Lecoq *et al.* (2004) nominally appear too large for asymptotic treatment with the shear-flow limit of the current domain-perturbation theory. However, as an heuristic approach, if rational approximations are used to the two-term protrusion length polynomials and the smallest amplitude ($\epsilon = 1.14$) 'Topography $\mathcal{B}$' discussed in tables 1 and 3 of that work is studied, a prediction $L_{eff} = 0.51$ is obtained following the procedure for interpreting their squeezed-film rather than shear-flow experimental data discussed in this study, whereas $L_{eff} = 0.47 \pm 0.02$ is reported experimentally. Thus, considering the error bounds, an error magnitude of 4.3 %–12.8 % between the rational approximation variant of the current theory and the experiment of Lecoq *et al.* (2004) is obtained. The semi-analytical model used by (Lecoq *et al.* 2004) to model their experimental data lacks a closed form, unlike the current model, but because of the inclusion of ϵ orders higher than two and the subsequent range extension through Euler transformation (Dyke 1984), it may be better suited for the specific large pattern size to pitch ratio used in their experiments, which might explain its better accuracy ($\pm 4.3\,\%$) than the current model.

Note that 'Topography $\mathcal{B}$' of Lecoq *et al.* (2004) is not related to the Topography B of the current work. Note also, excepting the scalloped topography, that all topographies studied as special cases in the current study are normalized for convenience to have $\max(g(x)) = 1$.

It can be pointed out in the current context that Bechert & Bartenwerfer (1989) use a slight generalization of the trapezoidal topography used here which has unequal flat zone length on its peak and valley and evaluate the protrusion height using Schwartz–Christoffel transformations. Closed-form results for S_1 and S_2 (not shown here for brevity) and therefore the protrusion height and large-H permeability can also be obtained for the same in a straightforward manner from the procedure used to calculate the trapezoidal topography entries in table 1.

5. Conclusions

Analytical predictions on the effective hydraulic permeability tensor in confined fluid flow with an arbitrarily shaped wall topography has been obtained using the assumption of small size-to-pitch ratio of the pattern. The flowing film of fluid may be driven either along or across the one-dimensional stripes by pressure while being enclosed between one smooth and one patterned wall or between two patterned walls, or between a free surface and a patterned wall or otherwise it could also be driven by a prescribed shear. In particular, applications of the last two configurations to slippery liquid-impregnated surfaces are demonstrated.

An important special case of the theoretical model is the large-height theory obtained through the approach of separating the effect of finite channel size into algebraic and exponentially decaying components. The large-height theory also implies that the pattern-averaged streamwise velocity for both longitudinal and transverse flow can be obtained by adapting the classical effective slip boundary condition for shear flows to the cross-channel variation of shear rate. Using the large channel height theory, a novel universal relationship connecting the two principal components of the permeability tensor is derived as a function of the root-mean-squared roughness (R_q) for channels with large (but finite) thickness to pattern pitch ratio. With this relationship, metrological characterization of the patterned surface along with knowledge of the permeability in any one direction will be sufficient to characterize the flow directed at an arbitrary angle to the stripes.

Two representative topographies formed by grooves in the shape of a phase-modulated sinusoid and triangles which differ in their degree of smoothness are studied as special cases. In particular, new closed-form analytical predictions for permeability with triangular, trapezoidal and scalloped wall grooves are obtained. The accuracy of the analytical predictions for these test problems are assessed against fully resolved numerical simulations for two representative topographies differing in their degree of smoothness. Corners of the form present in a triangular profile and even cusps of the form present in a scalloped profile are not found to be an impediment to accurate asymptotic prediction of hydraulic permeability, in contrast to an earlier suggestions from the literature (Kamrin *et al.* 2010). For the infinitely differentiable topography, the permeability is sensitive to the increase of the r.m.s. height of its profile as well as the increase in the number of peaks and troughs per period, when the former is fixed. In flow aligned along corrugations for either topography, the permeability may increase as well as decrease with increasing amplitude of corrugations depending on the channel size. In flow across corrugations, permeability always declines. Analytical approximations with an extended domain of numerical accuracy, which render the theory more useful at pattern sizes which are nominally 'not small', are also proposed.

Several applications of the theory to areas of technological importance, such as predicting the shear stability of liquid-infused surfaces and drag reduction, are demonstrated in the current study, along with an experimental comparison for trapezoidal grooves. The future work may attempt to generalize the findings for arbitrary topography shapes to other flow types (e.g. electrokinetic flow (Datta & Choudhary 2013; Ghosh & Chakraborty 2015)), allow the fluid to undergo hydrodynamic slippage, treat flows with inertia (Tuck & Kouzoubov 1995) and stratified two-phase flows (Wexler *et al.* 2015) for lubricant-impregnated textured surfaces. A formalism connecting the modelling of wetted surfaces to that of superhydrophobic surfaces of similar shape, e.g. the trapezoidal shapes of the current study and Zhou *et al.* (2013), for which a heuristic foundation is already laid by Mongruel *et al.* (2013), would also be welcome.

Declaration of interests

The authors report no conflict of interest.

Appendix A. Expressions used for predicting channel height effects in pressure-driven flow with one patterned and one no-slip wall

The constants and functions introduced in (3.14*f*) are given by

$$S_n(Y) = \mathrm{e}^{-|n|Y} - (1+2|n|H)\mathrm{e}^{-2|n|H}\mathrm{e}^{|n|Y} + 2|n|Y\mathrm{e}^{-2|n|H}\mathrm{e}^{|n|Y}, \tag{A 1a}$$

$$T_n(Y) = Y\mathrm{e}^{-|n|Y} - 2|n|H^2\mathrm{e}^{-2|n|H}\mathrm{e}^{|n|Y} + Y(-1+2|n|H)\mathrm{e}^{-2|n|H}\mathrm{e}^{|n|Y}, \tag{A 1b}$$

$$C_{1n} = -\frac{T_n(0)g_n}{2(T_n(0)S_n'(0) - T_n'(0)S_n(0))}, \tag{A 1c}$$

$$D_{1n} = \frac{S_n(0)g_n}{2(T_n(0)S_n'(0) - T_n'S_n(0))}. \tag{A 1d}$$

Appendix B. Transverse permeability in free surface and forced shear confined flows with finite channel size effects

With the mean line of topography pattern at $Y = 0$, if either a zero shear surface (such as an undisturbed interface of a flowing fluid with another quiescent fluid of

lower viscosity) exists at $y=H$ or an identically patterned wall exists at $Y=2H$, K_{pzs} gives the normalized permeability of the H thick film for the former case and a $2H$ thick film for the latter case. The permeability of the purely shear-driven flow with prescribed shear at $y=H$ is given by K_s. The finite-H expressions are as follows:

$$K_{pzs}^{\perp} = 1 - 6\alpha^2(2HC_s^{\perp} - 2D_s^{\perp} + S_2), \tag{B 1a}$$

$$K_s^{\perp} = 1 - 2\alpha^2(4HC_s^{\perp} - 2D_s^{\perp} - S_2), \tag{B 1b}$$

$$C_s^{\perp} = \frac{1}{2}\sum_{n\neq 0}^{\infty}(C_{1n}S_n''(0) + D_{1n}T_n''(0))g_n, \tag{B 2a}$$

$$D_s^{\perp} = -\frac{1}{2}\sum_{n\neq 0}^{\infty}(C_{1n}S_n'(0) + D_{1n}T_n'(0))g_n - \frac{S_2}{2}, \tag{B 2b}$$

with S_2 as defined in (3.6*d*). The constants and functions required by (B 2) are

$$C_{1n} = -\frac{T_n(0)g_n}{(T_n(0)S_n'(0) - T_n'(0)S_n(0))}, \tag{B 3a}$$

$$D_{1n} = \frac{S_n(0)g_n}{(T_n(0)S_n'(0) - T_n'(0)S_n(0))}, \tag{B 3b}$$

$$S_n(Y) = \mathrm{e}^{-|n|Y} - \mathrm{e}^{-2|n|H}\mathrm{e}^{|n|Y}, \tag{B 4a}$$

$$T_n(Y) = Y\mathrm{e}^{-|n|Y} - 2|n|H\mathrm{e}^{-2|n|H}\mathrm{e}^{|n|Y} + Y\mathrm{e}^{-2|n|H}\mathrm{e}^{|n|Y}. \tag{B 4b}$$

REFERENCES

ABRAMOWITZ, M. & STEGUN, I. A. 1964 *Handbook of Mathematical Functions: With Formulas, Graphs, and Mathematical Tables*. Courier Corporation.

AJDARI, A. 2001 Transverse electrokinetic and microfluidic effects in micropatterned channels: lubrication analysis for slab geometries. *Phys. Rev.* E **65** (1), 016301.

ALAMÉ, K. & MAHESH, K. 2019 Wall-bounded flow over a realistically rough superhydrophobic surface. *J. Fluid Mech.* **873**, 977–1019.

ANNEPU, H., SARKAR, J. & BASU, S. 2014 Pattern formation in soft elastic films cast on periodically corrugated surfaces – a linear stability and finite element analysis. *Model. Simul. Mater. Sci. Engng* **22** (5), 055003.

ASAKO, Y. & FAGHRI, M. 1987 Finite-volume solutions for laminar flow and heat transfer in a corrugated duct. *Trans. ASME J. Heat Transfer* **109** (3), 627–634.

ASMOLOV, E. S., BELYAEV, A. V. & VINOGRADOVA, O. I. 2011 Drag force on a sphere moving toward an anisotropic superhydrophobic plane. *Phys. Rev.* E **84** (2), 026330.

ASMOLOV, E. S., DUBOV, A. L., NIZKAYA, T. V., KUEHNE, A. J. C. & VINOGRADOVA, O. I. 2015 Principles of transverse flow fractionation of microparticles in superhydrophobic channels. *Lab on a Chip* **15** (13), 2835–2841.

ASMOLOV, E. S., NIZKAYA, T. V. & VINOGRADOVA, O. I. 2018 Enhanced slip properties of lubricant-infused grooves. *Phys. Rev.* E **98**, 033103.

ASMOLOV, E. S., SCHMIESCHEK, S., HARTING, J. & VINOGRADOVA, O. I. 2013*a* Flow past superhydrophobic surfaces with cosine variation in local slip length. *Phys. Rev.* E **87**, 023005.

ASMOLOV, E. S. & VINOGRADOVA, O. I. 2012 Effective slip boundary conditions for arbitrary one-dimensional surfaces. *J. Fluid Mech.* **706**, 108–117.

ASMOLOV, E. S., ZHOU, J., SCHMID, F. & VINOGRADOVA, O. I. 2013*b* Effective slip-length tensor for a flow over weakly slipping stripes. *Phys. Rev.* E **88**, 023004.

BAZANT, M. Z. & VINOGRADOVA, O. I. 2008 Tensorial hydrodynamic slip. *J. Fluid Mech.* **613**, 125–134.

BECHERT, D. W. & BARTENWERFER, M. 1989 The viscous flow on surfaces with longitudinal ribs. *J. Fluid Mech.* **206**, 105–129.

CANUTO, C., HUSSAINI, M., QUARTERONI, A. & ZANG, T. A. J. 1987 *Spectral Methods in Fluid Dynamics (Scientific Computation)*. Springer.

CHAKRABORTY, S. 2007 Towards a generalized representation of surface effects on pressure-driven liquid flow in microchannels. *Appl. Phys. Lett.* **90** (3), 034108.

CHANG, J., JUNG, T., CHOI, H. & KIM, J. 2019 Predictions of the effective slip length and drag reduction with a lubricated micro-groove surface in a turbulent channel flow. *J. Fluid Mech.* **874**, 797–820.

CHOI, H., MOIN, P. & KIM, J. 1993 Direct numerical simulation of turbulent flow over riblets. *J. Fluid Mech.* **255**, 503–539.

CHOI, C.-H., ULMANELLA, U., KIM, J., HO, C.-M. & KIM, C.-J. 2006 Effective slip and friction reduction in nanograted superhydrophobic microchannels. *Phys. Fluids* **18** (8), 087105.

CHOUDHARY, R., BHAKAT, T., SINGH, R. K., GHUBADE, A., MANDAL, S., GHOSH, A., RAMMOHAN, A., SHARMA, A. & BHATTACHARYA, S. 2011 Bilayer staggered herringbone micro-mixers with symmetric and asymmetric geometries. *Microfluid Nanofluid* **10** (2), 271–286.

CHU, K.-H. W. 1996 Stokes slip flow between corrugated walls. *Z. Angew. Math. Phys.* **47** (4), 591–599.

DATTA, S. & CHOUDHARY, J. N. 2013 Effect of hydrodynamic slippage on electro-osmotic flow in zeta potential patterned nanochannels. *Fluid Dyn. Res.* **45** (5), 055502.

DEVASENATHIPATHY, S., SANTIAGO, J. G. & TAKEHARA, K. 2002 Particle tracking techniques for electrokinetic microchannel flows. *Analyt. Chem.* **74** (15), 3704–3713.

DEWANGAN, M. K. & DATTA, S. 2018 Flow through microchannels with topographically patterned wall: a spectral theory for arbitrary groove depths. *Eur. J. Mech. (*B*/Fluids)* **70**, 73–84.

DEWANGAN, M. K. & DATTA, S. 2019 Improved asymptotic predictions for the effective slip over a corrugated topography. *Appl. Math. Model.* **72**, 247–258.

DEY, P., SAHA, S. K. & CHAKRABORTY, S. 2018 Microgroove geometry dictates slippery hydrodynamics on superhydrophobic substrates. *Phys. Fluids* **30** (12), 122007.

DUBOV, A. L., NIZKAYA, T. V., ASMOLOV, E. S. & VINOGRADOVA, O. I. 2018 Boundary conditions at the gas sectors of superhydrophobic grooves. *Phys. Rev. Fluids* **3** (1), 014002.

DUNLOP, J. 2017 *Telecommunications Engineering*. Routledge.

DYKE, M. V. 1984 Computer-extended series. *Annu. Rev. Fluid Mech.* **16** (1), 287–309.

EINZEL, D., PANZER, P. & LIU, M. 1990 Boundary condition for fluid flow: curved or rough surfaces. *Phys. Rev. Lett.* **64**, 2269–2272.

FEUILLEBOIS, F., BAZANT, M. Z. & VINOGRADOVA, O. I. 2009 Effective slip over superhydrophobic surfaces in thin channels. *Phys. Rev. Lett.* **102**, 026001.

FEUILLEBOIS, F., BAZANT, M. Z. & VINOGRADOVA, O. I. 2010 Transverse flow in thin superhydrophobic channels. *Phys. Rev.* E **82**, 055301.

GAMRAT, G., FAVRE-MARINET, M., LE PERSON, S., BAVIERE, R. & AYELA, F. 2008 An experimental study and modelling of roughness effects on laminar flow in microchannels. *J. Fluid Mech.* **594**, 399–423.

GHOSAL, S. 2002 Lubrication theory for electroosmotic flow in a channel of slowly varying cross-section and wall charge. *J. Fluid Mech.* **459**, 103–128.

GHOSH, U. & CHAKRABORTY, S. 2015 Electroosmosis of viscoelastic fluids over charge modulated surfaces in narrow confinements. *Phys. Fluids* **27** (6), 062004.

GUO, L., CHEN, S. & ROBBINS, M. O. 2016 Effective slip boundary conditions for sinusoidally corrugated surfaces. *Phys. Rev. Fluids* **1** (7), 074102.

HINCH, E. J. 1991 *Perturbation Methods*. Cambridge University Press.

HOCKING, L. M. 1976 A moving fluid interface on a rough surface. *J. Fluid Mech.* **76**, 801–817.

IMANI, B. M. & ELBESTAWI, M. A. 2001 Geometric simulation of ball-end milling operations. *J. Manufacturing Sci. Engng* **123** (2), 177–184.

KAMRIN, K., BAZANT, M. Z. & STONE, H. A. 2010 Effective slip boundary conditions for arbitrary periodic surfaces: the surface mobility tensor. *J. Fluid Mech.* **658**, 409–437.

KUMAR, A., DATTA, S. & KALYANASUNDARAM, D. 2016 Permeability and effective slip in confined flows transverse to wall slippage patterns. *Phys. Fluids* **28** (8), 082002.

LAUGA, E. & STONE, H. A. 2003 Effective slip in pressure-driven Stokes flow. *J. Fluid Mech.* **489**, 55–77.

LECOQ, N., ANTHORE, R., CICHOCKI, B., SZYMCZAK, P. & FEUILLEBOIS, F. 2004 Drag force on a sphere moving towards a corrugated wall. *J. Fluid Mech.* **513**, 247–264.

LI, C. & CHEN, T. 2005 Simulation and optimization of chaotic micromixer using lattice Boltzmann method. *Sensors Actuators* B **106** (2), 871–877.

LUCHINI, P. 2013 Linearized no-slip boundary conditions at a rough surface. *J. Fluid Mech.* **737**, 349–367.

LUCHINI, P., MANZO, F. & POZZI, A. 1991 Resistance of a grooved surface to parallel flow and cross-flow. *J. Fluid Mech.* **228**, 87–109.

MCCARTHY, K. P., RING, L. & RANA, B. S. 2010 Anatomy of the mitral valve: understanding the mitral valve complex in mitral regurgitation. *Eur. J. Echocardiography* **11** (10), i3–i9.

MIKSIS, M. J. & DAVIS, S. H. 1994 Slip over rough and coated surfaces. *J. Fluid Mech.* **273**, 125–139.

MONGRUEL, A., CHASTEL, T., ASMOLOV, E. S. & VINOGRADOVA, O. I. 2013 Effective hydrodynamic boundary conditions for microtextured surfaces. *Phys. Rev.* E **87** (1), 011002.

NIZKAYA, T. V., ASMOLOV, E. S., ZHOU, J., SCHMID, F. & VINOGRADOVA, O. I. 2015 Flows and mixing in channels with misaligned superhydrophobic walls. *Phys. Rev.* E **91** (3), 033020.

PANZER, P., LIU, M. & EINZEL, D. 1992 The effects of boundary curvature on hydrodynamic fluid flow: calculation of slip lengths. *Intl J. Mod. Phys.* B **6** (20), 3251–3278.

PARMAR, V., KUMAR, A., SANKAR, M. M., DATTA, S., PRAKASH, G. V., MOHANTY, S. & KALYANASUNDARAM, D. 2018 Oxidation facilitated antimicrobial ability of laser micro-textured titanium alloy against gram-positive staphylococcus aureus for biomedical applications. *J. Laser Appl.* **30**, 032001.

QI, C. & NG, C.-O. 2015 Electroosmotic flow of a power-law fluid in a slit microchannel with gradually varying channel height and wall potential. *Eur. J. Mech. (B/Fluids)* **52**, 160–168.

RANGSTEN, P., HEDLUND, C., KATARDJIEV, I. V. & BÄCKLUND, Y. 1998 Etch rates of crystallographic planes in *Z*-cut quartz-experiments and simulation. *J. Micromech. Microengng* **8** (1), 1.

RICHARDSON, S. 1973 On the no-slip boundary condition. *J. Fluid Mech.* **59** (4), 707–719.

SARKAR, K. & PROSPERETTI, A. 1996 Effective boundary conditions for Stokes flow over a rough surface. *J. Fluid Mech.* **316**, 223–240.

SCHMIESCHEK, S., BELYAEV, A. V., HARTING, J. & VINOGRADOVA, O. I. 2012 Tensorial slip of superhydrophobic channels. *Phys. Rev.* E **85**, 016324.

SCHOLLE, M., WIERSCHEM, A. & AKSEL, N. 2004 Creeping films with vortices over strongly undulated bottoms. *Acta Mechanica* **168** (3–4), 167–193.

SCHÖNFELD, F. & HARDT, S. 2004 Simulation of helical flows in microchannels. *AIChE J.* **50** (4), 771–778.

SHARMA, H., GADDAM, A., AGRAWAL, A. & JOSHI, S. S. 2019 Slip flow through microchannels with lubricant-infused bi-dimensional textured surfaces. *Microfluid Nanofluid* **23** (2), 28.

SISAVATH, S., AL-YAARUBI, A., PAIN, C. C. & ZIMMERMAN, R. W. 2003 A simple model for deviations from the cubic law for a fracture undergoing dilation or closure. In *Thermo-Hydro-Mechanical Coupling in Fractured Rock*, pp. 1009–1022. Springer.

SLOANE, N. J. A. 2019 The on-line encyclopedia of integer sequences. Available at: https://oeis.org/A002117.

SOLOMON, B. R., CHEN, X., RAPOPORT, L., HELAL, A., MCKINLEY, G. H., CHIANG, Y.-M. & VARANASI, K. K. 2018 Enhancing the performance of viscous electrode-based flow batteries using lubricant-impregnated surfaces. *ACS Appl. Energy Mater.* **1** (8), 3614–3621.

SONG, D., DANIELLO, R. J. & ROTHSTEIN, J. P. 2014 Drag reduction using superhydrophobic sanded Teflon surfaces. *Exp. Fluids* **55** (8), 1783.

STONE, H. A., STROOCK, A. D. & AJDARI, A. 2004 Engineering flows in small devices. *Annu. Rev. Fluid Mech.* **36**, 381–411.

STROOCK, A. D., DERTINGER, S. K., WHITESIDES, G. M. & AJDARI, A. 2002 Patterning flows using grooved surfaces. *Analyt. Chem.* **74** (20), 5306–5312.

STROOCK, A. D. & MCGRAW, G. J. 2004 Investigation of the staggered herringbone mixer with a simple analytical model. *Phil. Trans. R. Soc. Lond.* A **362** (1818), 971–986.

SUN, R. & NG, C.-O. 2017 Effective slip for flow through a channel bounded by lubricant-impregnated grooved surfaces. *Theor. Comput. Fluid Dyn.* **31** (2), 189–209.

TAVAKOL, B., FROEHLICHER, G., HOLMES, D. P. & STONE, H. A. 2017 Extended lubrication theory: improved estimates of flow in channels with variable geometry. *Proc. R. Soc. Lond.* A **473** (2206), 20170234.

TAYLOR, G. I. 1971 A model for the boundary condition of a porous material. Part 1. *J. Fluid Mech.* **49** (2), 319–326.

TUCK, E. O. & KOUZOUBOV, A. 1995 A laminar roughness boundary condition. *J. Fluid Mech.* **300**, 59–70.

VAN DYKE, M. 1987 Slow variations in continuum mechanics. *Adv. Appl. Mech.* **25**, 1–45.

VASUDEVIAH, M. & BALAMURUGAN, K. 1999 Stokes slip flow in a corrugated pipe. *Intl J. Engng Sci.* **37** (12), 1629–1641.

VINOGRADOVA, O. I. & BELYAEV, A. V. 2011 Wetting, roughness and flow boundary conditions. *J. Phys.: Condens. Matter* **23** (18), 184104.

WANG, C. Y. 2003 Flow over a surface with parallel grooves. *Phys. Fluids* **15** (5), 1114–1121.

WANG, C. Y. 2010 Shear flow over a wavy surface with partial slip. *Trans. ASME J. Fluids Engng* **132** (8), 084503.

WANG, C. Y. 2011 On Stokes slip flow through a transversely wavy channel. *Mech. Res. Commun.* **38** (3), 249–254.

WARE, C. S., SMITH-PALMER, T., PEPPOU-CHAPMAN, S., SCARRATT, L. R. J., HUMPHRIES, E. M., BALZER, D. & NETO, C. 2018 Marine antifouling behavior of lubricant-infused nanowrinkled polymeric surfaces. *ACS Appl. Mater. Interfaces* **10** (4), 4173–4182.

WATSON, G. N. 1995 *A Treatise on the Theory of Bessel Functions*. Cambridge University Press.

WEXLER, J. S., JACOBI, I. & STONE, H. A. 2015 Shear-driven failure of liquid-infused surfaces. *Phys. Rev. Lett.* **114**, 168301.

WHITEHOUSE, D. J. 1994 *Handbook of Surface Metrology*. CRC Press.

WIERSCHEM, A., SCHOLLE, M. & AKSEL, N. 2003 Vortices in film flow over strongly undulated bottom profiles at low Reynolds numbers. *Phys. Fluids* **15** (2), 426–435.

WONG, T.-S., KANG, S. H., TANG, S. K. Y., SMYTHE, E. J., HATTON, B. D., GRINTHAL, A. & AIZENBERG, J. 2011 Bioinspired self-repairing slippery surfaces with pressure-stable omniphobicity. *Nature* **477** (7365), 443–447.

YBERT, C., BARENTIN, C., COTTIN-BIZONNE, C., JOSEPH, P. & BOCQUET, L. 2007 Achieving large slip with superhydrophobic surfaces: scaling laws for generic geometries. *Phys. Fluids* **19** (12), 123601.

YUTAKA, A., HIROSHI, N. & FAGHRI, M. 1988 Heat transfer and pressure drop characteristics in a corrugated duct with rounded corners. *Intl J. Heat Mass Transfer* **31** (6), 1237–1245.

ZHOU, J., ASMOLOV, E. S., SCHMID, F. & VINOGRADOVA, O. I. 2013 Effective slippage on superhydrophobic trapezoidal grooves. *J. Chem. Phys.* **139** (17), 174708.